Project No. 13-5531

High Fidelity Ion Beam Simulation of High Dose Neutron Irradiation

Integrated Research Project

Gary Was
University of Michigan

Collaborators
Pennsylvania State University
University of California, Berkeley
University of California, Santa Barbara
University of South Carolina
University of Tennessee
University of Wisconsin

William Corwin, Federal POC
Jeremy Busby, Technical POC

NEUP Nuclear Energy University Programs
U.S. Department of Energy

Final Technical Progress Report
COVER PAGE

Federal Agency to which Report is submitted: DOE NE – NEUP

Recipient: University of Michigan
Award Number: DE-NE0000639
Project Title: High Fidelity Ion Beam Simulation of High Dose Neutron Irradiation
Project Period: March 2014 to December 2017

Principal Investigator: Gary S. Was, University of Michigan, gsw@umich.edu

Date of Report: March 31, 2018
Covering Period: March 1, 2014 to December 31, 2017
Report Frequency: Quarterly

PIs:
Z. Jiao, E. Marquis, University of Michigan
B. Wirth, D. Xu, University of Tennessee
A. Motta, Penn State University
D. Morgan, University of Wisconsin
D. Kaoumi, University of South Carolina
P. Hosemann, University of California, Berkeley
G. R. Odette, University of California, Santa Barbara
K. Field, Oak Ridge National Laboratory
S. Tumey, Lawrence Livermore National Laboratory

Partners:
S. Maloy, Los Alamos National Laboratory
M. Kirk, Argonne National Laboratory
J. Cole, Idaho National Laboratory
M. Hackett, B. Hilton, TerraPower LLC
R. Pathania, EPRI
G. Burke, M. Preuss, University of Manchester
S. Roberts, University of Oxford
L. Fournier, Areva
M. Daymond, University of Queens
M. Le Flem, CEA

OBJECTIVES AND GOALS

Project Objective: The objective of this proposal is to ***demonstrate the capability to predict the evolution of microstructure and properties of structural materials in-reactor and at high doses, using ion irradiation as a surrogate for reactor irradiations.*** "Properties" includes both physical properties (irradiated microstructure) and the mechanical properties of the material. Demonstration of the capability to predict properties has two components. One is ion irradiation of a set of alloys to yield an irradiated microstructure and corresponding mechanical behavior that are substantially the same as results from neutron exposure in the appropriate reactor environment. Second is the capability to predict the irradiated microstructure and corresponding mechanical behavior on the basis of improved models, validated against both ion and reactor irradiations and verified against ion irradiations. Taken together, achievement of these objectives will yield an enhanced capability for simulating the behavior of materials in reactor irradiations.

Project Goals:

1. The first thrust is the enhancement of MIBL to enable dual- and triple-beam ion irradiations under conditions tailored to achieve a microstructure that is representative of exposure from neutrons in the appropriate reactor environment. Bulk sample ion irradiations will be conducted at the Michigan Ion Beam Laboratory with complementary single ion irradiations at LLNL. In-situ ion irradiations will be conducted in the IVEM to study the temporal evolution of the microstructure in the low dose regime, and to serve as benchmarks for the modeling activity. TerraPower, LLC will arrange for return shipment of all samples irradiated in BOR-60 for comparison with ion irradiations.
2. The goal consists of characterization and modeling of the irradiated microstructures. Characterization will be done by multiple techniques but principally by TEM and APT, and work flow and results will be managed by the Thrust 2 Leads; Arthur Motta and Brian Wirth. Neutron irradiated samples will also be characterized by several participating institutions. Experimental characterization and microstructure modeling will go hand in hand under Thrust 2 with A. Motta directing the workflow for the characterization effort and B. Wirth doing the same for the modeling effort.
3. The third major element of the program is the determination of mechanical properties of reactor- and ion- irradiated samples and the development of predictive models to tie the irradiated microstructure to their properties (Thrust 3). Samples irradiated at MIBL and in BOR-60 will be made available to UCB and UCSB for mechanical property characterization. Results will be used along with those from the microstructure characterization program in Thrust 2 to benchmark microstructure-property models on reactor-irradiated samples for use on ion irradiated samples, from which mechanical property data is harder to acquire.
4. A set of supporting activities (Thrust 4) will be conducted that will serve to engage all participants, and also those from the radiation effects community that are not a part of this IRP. These include establishment of working groups on Ion Irradiation and on Sample Preparation and Analysis and a Workshop on Emulating Reactor Irradiation with Ion Irradiation.

MAJOR ACCOMPLISHMENTS

F*acilities*

- Designed, constructed, and verified the equipment necessary for multiple ion beam irradiations for the study of radiation damage in materials.
- Resolved the problem of carbon contamination in ion irradiation experiments.
- Established new collaborations with industry and research institutions to use the extensive capabilities of the laboratory.

Irradiation campaign

- Irradiation campaign started on 21 capsules in the BOR-60 reactor with 44 discs of up to 15 alloys per capsule at 4 temperatures and 5 doses. In-situ ion irradiations were conducted on 4 alloys with up to 5 different temperature conditions and continually monitored up to 30 dpa. Single ion irradiations were performed on 4 alloys with up to 4 different temperature conditions and 3 distinct doses including one high energy ion irradiation. Dual ion irradiations were completed for 4 alloys with up to 9 different temperatures up to 2 doses with up to 2 different helium co-injection rates.

Irradiated microstructure characterization

- Dislocation loops were observed at 376°C-415°C while only network dislocations were observed at 460°C and 524°C. The dominance of network dislocations at high temperatures of 460°C and 524°C is consistent with observations of F-M alloys in FFTF irradiations. Dislocation loops saturated at 17.1 dpa at 376°C. Dislocation loops were mainly a<100> type in BOR60 irradiated T91 which is also consistent with observations in FFTF irradiation.
- Cavities were observed in BOR60 irradiated T91 at all examined irradiation conditions. A bimodal cavity distribution was observed with a high density of small bubbles less than 2 nm in the temperature range 376-415°C. Only small bubbles were observed at 460°C and 524°C. Voids (cavities > 2 nm) were in the nucleation stage at 17.1 dpa and the number density as well as swelling increased with irradiation dose at 376-378°C.
- The dominant radiation-induced precipitates were the Ni/Si-rich G-phase precipitates in BOR60 irradiated T91. The average size and volume fraction increased slightly with dose and temperature but a continued increase in volume fraction was not expected at much higher doses due to the low bulk Ni content. The absence of Ni/Si-rich precipitates at 460°C was likely due to the lack of dislocation loops as additional nucleation sites. No Ni/Si-rich precipitates were observed at 524°C due to the minimal RIS of Ni and Si at the temperature. Cu-rich precipitates were observed in BOR60 irradiated T91 at 376-415°C.
- Enrichment of Cr, Ni and Si at the grain boundary occurred at all doses and temperatures. At a temperature of 376°C RIS appeared to saturate at 17.1 dpa. Cr enrichment peaked at a temperature of 460°C, and Ni and Si enrichments peaked at lower temperatures.
- Temperature dependence of microstructural features in dual ion irradiated T91 was determined. The relationship between temperature and cavity evolution in dual ion irradiated T91 exhibited the expected trends of a bell-shaped curve for cavity density and an increasing cavity diameter with temperature.

- Temperature dependence of microstructural features in dual ion irradiated T91 was determined. The relationship between temperature and cavity evolution in dual ion irradiated T91 exhibited the expected trends of a bell-shaped curve for cavity density and an increasing cavity diameter with temperature.
- The temperature shift for dual ion irradiation was determined by matching major microstructural features of BOR-60 irradiated T91. A temperature shift of ~60°C for dual ion irradiation was found to result in both a qualitative and quantitative match of cavities in BOR-60 irradiated T91 heat 30176.
- Irradiation induced dislocation loop population in Ferritic/Martensitic steels T91 and HT9: In-situ ion irradiation vs. Ex-situ (bulk) single ion irradiation vs. neutron irradiation. Observations made on the in-situ irradiations were comparable with the measurements done on the ex-situ irradiation experiments, i.e. a <100> type loops were also found to be the predominant type for both the bulk (ex-situ) ion irradiation and the BOR-60 neutron irradiation F/M steel HT9 at the doses investigated (17-33dpa)
- Radiation-induced precipitation and segregation in Ferritic/Martensitic steel HT9: Ex-situ (bulk) ion irradiation vs. neutron irradiation. The observations of the ion irradiations were comparable with those of neutron irradiated HT9, in terms of radiation-induced precipitation of G-phase and radiation-induce segregation in the vicinity of cavities. However, α' (Cr-rich) precipitation were only observed in neutron irradiated HT9, indicating that lower dose rates should be investigated under ion irradiation.
- G-phase and α' precipitates were observed BOR60 irradiated HT9 from 376 to 426ºC but they were not observed at 460□C. However, small clusters of Ni, Si, and Mn atoms were observed at 450 ºC in the Dual ion irradiated sample. The number density and radius of G-phase precipitates in BOR60 irradiated HT9 did not show significant variance with increasing temperature or dose. The dual-beam ion irradiated HT9 sample has the highest number density and radius compared to the BOR60 irradiated samples.
- The irradiation induced features formed on ion irradiated and neutron irradiated alloy 800H after 10-20 dpa were similar. These included both 111 and 110 type loops, irradiation induced segregation and formation of voids.
- Using the appropriate temperature shift the loop microstructure in alloy 800H was qualitatively and quantitatively reproduced using ion irradiation to a dose of ~ 20 dpa.
- The irradiation induced features seen after ion irradiation to ~ 20 dpa of the Fe-21Cr-32Ni model alloy were quite similar to the sister commercial alloy 800H, in terms of faulted loop density and diameter. Also, the unfaulting mechanism identified was operational in both alloys, leading to the formation of a dense dislocation network.
- The irradiation induced grain boundary segregation was observed to be qualitatively the same in ion irradiated Fe-21Cr-32Ni model alloy as in 800H.
- Voids were observed in the ion irradiated microstructures of both Fe-21Cr-32Ni model alloy and 800H, showing lower levels than those under neutron irradiation.

Irradiated microstructure modeling

- Cluster dynamics modeling of defect cluster evolution in a model, body centered cubic metal demonstrated ability to tailor ion irradiation conditions to exactly match neutron irradiation effects

- Cluster dynamics model developed that accurately predicts Mn-Ni-Si precipitate evolution in irradiated body-centered cubic Fe-based steels under neutron and ion irradiation conditions
- Demonstrated the important role of cavity sink strength and bias on predicting void swelling incubation dose in irradiated Fe-Cr alloys
- Demonstrated the importance of cascade overlap-induced recombination mechanism on accurately predicting defect microstructure evolution in irradiated alloy 800H

Mechanical properties of irradiated materials

- Established correlations between nano- and macro-scale mechanical properties utilizing neutron-irradiated samples from ATR and BOR60. Hardness (H) from nanoindentation; tensile yield, flow, and ultimate stresses (σ_y, σ_{flow}, and σ_{uts}) from tensile testing; and shear yield and max (τ_y and τ_{max}) from shear punch testing were all directly measured on the same samples. Methods to extract both tensile and shear macro-scale properties from nanohardness were developed.
- Evaluated size effects in both indentation and micro-pillar compression testing utilizing neutron- and ion-irradiated materials over relevant temperature ranges and compared results trends in macro-scale properties.
- Developed microstructure-based predictions of hardening on irradiated steels and validated this method utilizing neutron-irradiated sample data.

1. Thrust 1: Facility Enhancement and Irradiation Plan

1.1 Facilities Enhancement (Was Group, University of Michigan)

Major accomplishments and outcomes of the Facility Enhancement

1. **Designed, constructed, and verified the equipment necessary for multiple ion beam irradiations for the study of radiation damage in materials.**
2. **Resolved the problem of carbon contamination in ion irradiation experiments.**
3. **Established new collaborations with industry and research institutions to use the extensive capabilities of the laboratory.**

Over the course of this project, the Michigan Ion Beam Laboratory was transformed. In December 2013, the Michigan Ion Beam Laboratory was deconstructed. A new accelerator arrived in February 2014 to complement the two accelerators already in the laboratory, and the laboratory was expanded beyond the original space to include a room dedicated to target stations, Figure 1.1. With the construction of new beamlines, the capability to perform proton irradiation experiments was regained in June 2014 with heavy ion irradiation capability restored in October 2014. A year later in October 2015, the first multiple ion beam irradiation experiment on commercial steels was performed in a custom target chamber connected to new beamlines using iron ions to induce damage in the material and simultaneously co-injecting helium ions to simulate transmutation gas buildup, with new procedures to ensure the highest quality of ion irradiation experiments. In under two years, the Michigan Ion Beam Laboratory was enhanced to become a world class facility for the study of radiation damage in materials.

The novelty of this facility enhancement stems from establishing the capability to perform well controlled multiple ion beam irradiation experiments for the purpose of emulating reactor irradiated microstructures. Careful alignment of the beamlines between the high energy bending magnets and the target was necessary to converge ion beams from multiple accelerators to a single target. New measurement techniques of the ion flux intensity were developed to ensure the spatial uniformity of the ion beams across the irradiated area using common beamline diagnostic components of slit apertures and a Faraday cup. The temperature of the ion irradiation stage is controlled with minimal variability using a combination of heating from a resistive element in the metal alloy head and cooling with compressed air through channels machined into the stage head.

A large innovation in the enhancement of the facility was the development of a rotating thin foil energy degrader, a necessary component to control the beam energy below the minimum stable voltages of the accelerators. The foil is rotatable to increase the electronic energy loss and scattering of the beam by changing the path length of the beam through the foil. The ion flux from the foil degrader was benchmarked experimentally against the Stopping and Range of Ions in Matter (SRIM) program to determine the implantation distribution as a function of energy and position on the sample surface. By controlling the time spent at each angle during rotation, the depth of implantation can be manipulated to form any concentration profile of interest to the user, from following the heavy ion damage profile in a set gas/dpa ratio, or a flat profile for a specific concentration across the ion implantation range.

A distinguishing feature of multiple ion beam irradiations conducted in the Michigan Ion Beam Laboratory is the ability to control components remotely through an internet protocol network. This enabled all instruments in the laboratory (ion sources, accelerators, beamline components, and target chamber instrumentation) to be monitored and controlled remotely from the Control Room or from any computer on the lab network. Each accelerator has a single control computer for its set of components from ion source to target. After loading a set of samples onto the irradiation stage and pumping down the chamber, the remainder of the setup and execution of the irradiation experiment is controlled remotely. The liquid nitrogen cold trap maintains temperature using sensors to measure the remaining liquid in the dewar and refill automatically once the liquid reaches a set level. The heater and air cooling are controlled with a user interface with simultaneous read-back of the thermocouples and the thermal camera. Steering, focusing and alignment of the ion beams are verified using a marked grid of alumina. Analog signals from each device, such as the magnets, electrostatic steerers, and Faraday cups are digitized using embedded hardware. The digitization of the signals also allows selected signals to be logged in a database for recall or displayed in real time, ensuring the quality of multiple ion beam irradiations.

Critical to the success of ion irradiation as a radiation damage simulation tool is that the ion irradiated microstructure reflects the damage created by the ions and is not influenced by external factors such as incorporation of impurities into the sample during irradiation. During this project, mitigation techniques were developed to eliminate the widely experienced problem of carbon uptake in samples during ion irradiation. Standard cleaning techniques were inadequate to remove enough hydrocarbons to prevent cracking of carbon molecules under irradiation followed by adsorption and then absorption during irradiation. Plasma cleaning creates an active plasma in a remote chamber using radio frequency energy and transfers the active species to the cleaning chamber via gas flow. Room air acts as a source of oxygen to create reactive radicals and crack hydrocarbon chains, removing carbon incorporation into the sample by removing carbon from the sample and stage surfaces prior to irradiation. The liquid nitrogen cold trap provides approximately 800 cm^2 surface area to condensate any hydrocarbons in the vacuum chamber on the cold surface, preventing incorporation in the same during irradiation. Both plasma cleaning prior to irradiation and use of a liquid nitrogen cold trap during irradiation effectively removed or immobilized the hydrocarbons (Figure 1.2), allowing for high temperature irradiation without the uptake of carbon. An example of the difference in carbon uptake in the ferritic-martensitic steel HT9 is included in Figure 1.3. Uptake of carbon in ion irradiated samples was the result of adsorption under the beam of hydrocarbons that are present both in the vacuum system and on the surfaces of samples and mounting stages. This was the first report of complete elimination of carbon uptake for high fluence, high temperature ion irradiation of iron-base alloys.

The Michigan Ion Beam Laboratory will be used to investigate the effects of the gas/dpa ratio, temperature (cryogenic to 1200°C), damage (up to hundreds of dpa) and damage rate (10^{-5} to 10^{-3} dpa/s) on the evolution of irradiated microstructures up to high damage levels. Access to the multiple ion beam facility is available through the Nuclear Science User Facility (NSUF) platform enabling state of the art research with the extensive capabilities of the laboratory. The enhancement of the Michigan Ion Beam Laboratory encouraged collaborations from international research institutions (CEA in France and SCKCEN in Belgium) and industry

(EPRI and TerraPower, LLC) to perform multiple ion beam irradiations on structural materials and candidate materials for current and next generation reactors to high doses and high temperatures. Having multiple target chambers and high energy accelerators allows for multiple single ion beam irradiations to be performed simultaneously with completely different experimental conditions. The upgraded capability established as part of this project enables the community to advance materials research ahead of test reactors and deter potential in-reactor problems.

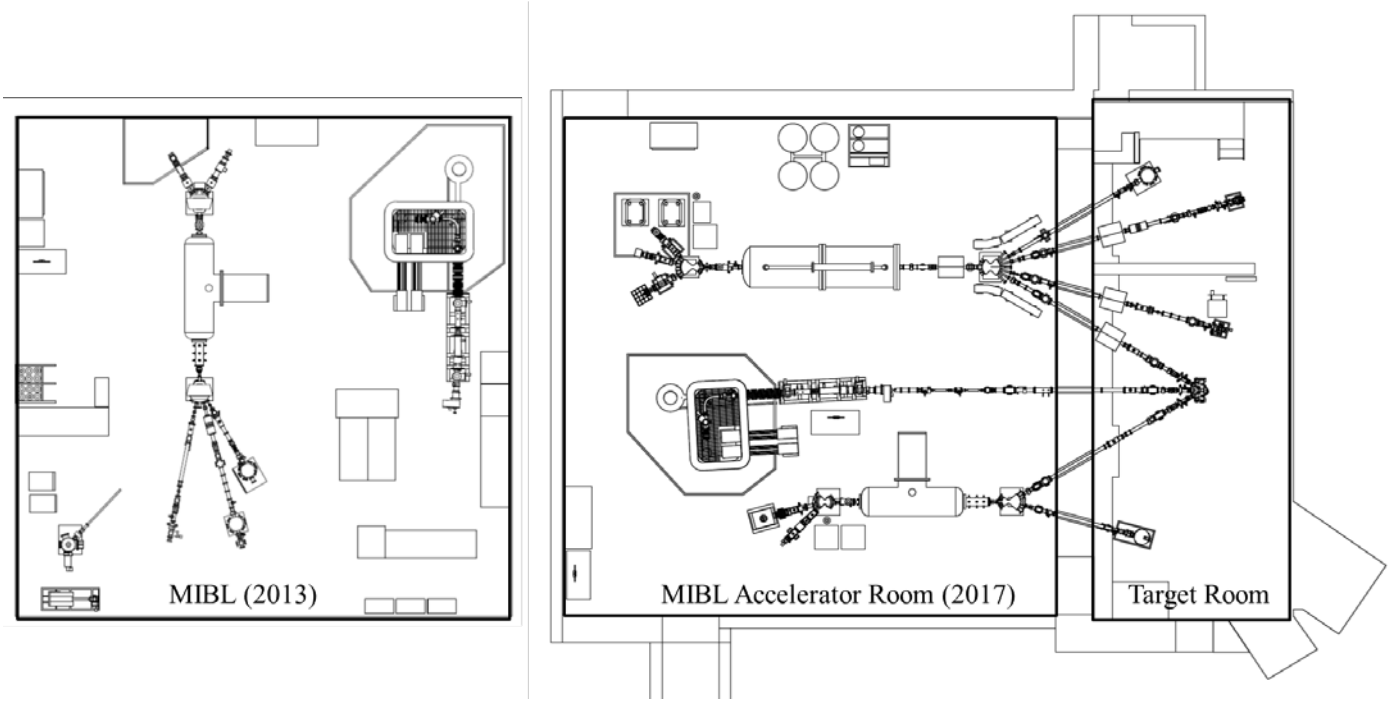

Figure 1.1. Schematics of the Michigan Ion Beam Laboratory before renovation (left) and after renovation (right) highlighting the expansion of the laboratory outside of its original space with the addition of the target room.

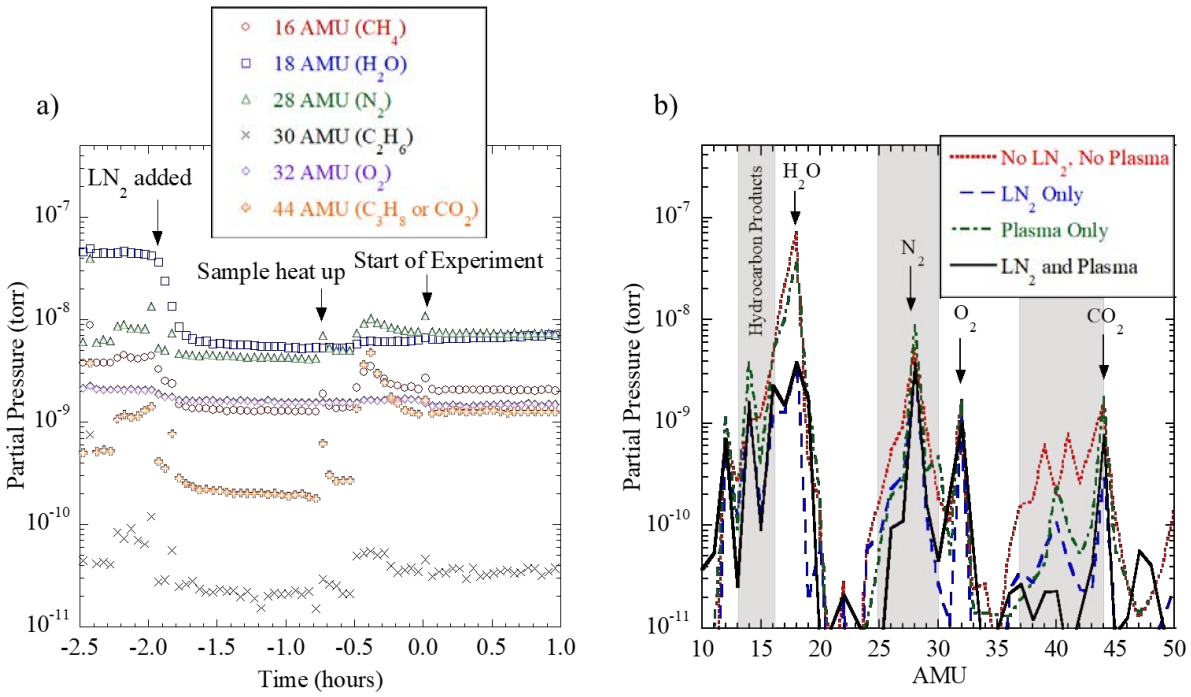

Figure 1.2. Partial pressures of selected gasses in the vacuum a) as a function of time after plasma cleaning and cooling of the cold trap, and b) as a function of amu for different procedures to reduce carbon contamination.

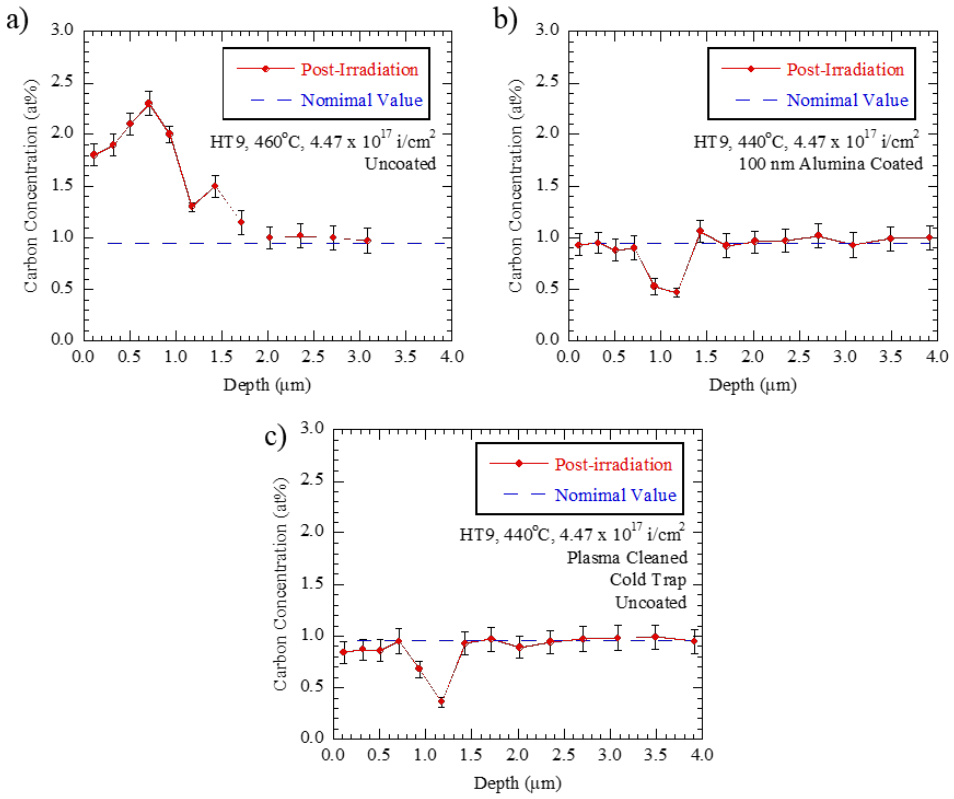

Figure 1.3. Carbon concentration profile for alloy HT9 following dual ion irradiation with 5 MeV Fe^{2+} to high dpa at 440°C or 460°C a) prior to institution of carbon control measures, b) with a 100 nm alumina coating as a diffusion barrier, and c) on a bare sample following plasma cleaning and the use of the cold trap.

1a.2 Neutron and Ion Irradiation

Major accomplishments of the Irradiation Campaign

1. **Irradiation campaign started on 21 capsules in the BOR-60 reactor with 44 discs of up to 15 alloys per capsule at 4 temperatures and 5 doses.**
2. **In-situ ion irradiations were conducted on 4 alloys with up to 5 different temperature conditions and continually monitored up to 30 dpa.**
3. **Single ion irradiations were performed on 4 alloys with up to 4 different temperature conditions and 3 distinct doses including one high energy ion irradiation.**
4. **Dual ion irradiations were completed for 4 alloys with up to 9 different temperatures up to 2 doses with up to 2 different helium co-injection rates.**

To demonstrate the capability to predict the evolution of microstructure and properties of structural materials in-reactor and at high doses, using ion irradiation as a surrogate for reactor irradiations, the evolution of the microstructure must be known from both ion and neutron irradiations. This project used four irradiation campaigns to evaluate the irradiated

microstructure of several materials: 1) neutron irradiation of capsules in the BOR-60 reactor, 2) in-situ ion irradiations in a transmission electron microscope, 3) single ion irradiations on bulk materials, 4) dual ion irradiations on bulk materials using the new capability developed in this project. A visual summary of all irradiations performed as part of this project is included in Figure 1.4, as a function of irradiation temperature and dose separated by austenitic alloys (800H, Fe21Cr32Ni) and ferritic-martensitic alloys (T91, HT9).

This project began with an ambitious and extensive neutron irradiation campaign. The neutron irradiation campaign started by sending 21 capsules to be irradiated in the BOR-60 reactor each with 44 discs of up to 15 alloys per capsule for irradiation in rigs to achieve irradiated microstructures at 4 temperatures and up to 5 doses ranging from 15 to 100 dpa. The capsules included simple materials (α-Fe), model alloys (Fe21Cr32Ni, Fe9Cr, Fe12Cr), commercial alloys (800H, T91, HT9), and advanced alloys (14YWT) irradiated at the same conditions. As part of this project, alloys from six capsules were examined, five capsules from 15-19 dpa and one capsule at 35 dpa. The neutron irradiation campaign coordinated efforts from Terrapower LLC, Los Alamos National Laboratory, Oak Ridge National Laboratory, Pacific Northwest National Laboratory, and the University of California – Berkeley to ship the samples to facilities where the irradiated microstructure and mechanical properties were characterized. The results from this characterization were presented in previous reports and a summary of the major accomplishments are included in a later section.

In-situ ion irradiations were conducted in the IVEM facility at Argonne National Laboratory to study the temporal evolution of the microstructure at low doses. In-situ ion irradiations on 4 alloys with up to 5 different temperature conditions and continually monitored from the start of irradiation up to 30 dpa. This work was driven primarily by Pennsylvania State University and North Carolina State University, focusing on austenitic alloys and ferritic-martensitic alloys respectively. In-situ ion irradiations were conducted across a wide range of temperatures to study dynamic defect interaction and determine the kinetic information necessary to benchmark modeling activity. In-situ irradiations of single ion irradiated austenitic alloys demonstrated the strong sink characteristics of the thin film geometry as irradiation induced cavities shrunk with increasing in-situ ion irradiation. The results from this project suggested in-situ irradiation is not an appropriate means of directly reproducing the irradiated microstructure, but rather should be used as an alternative way to subject the sample to irradiation to investigate the dynamics of defect formation and aggregation under different conditions complementary with modeling and bulk ion irradiations.

Before developing the capability to perform multiple ion beam irradiations, a series of single ion irradiations were conducted on bulk materials. Single ion irradiations were performed on 4 alloys (800H, Fe21Cr32Ni, T91, HT9) with up to 4 different temperature conditions per set of either austenitic or ferritic-martensitic alloys and 3 distinct doses from 1 to 20 dpa including one high energy ion irradiation. The results from these irradiations were compared with the in-situ ion irradiations conducted at similar damage rates and temperatures to determine the effects of the geometry differences (thin film vs. bulk) on the observed microstructural evolution. Significant characterization efforts on the dislocations, cavities, segregation, and precipitation behavior by Pennsylvania State University, University of Michigan, University of Manchester, and the Oxford University provided a large set of microstructural characterizations for the modeling of

mechanical properties at the University of California – Santa Barbara with micromechanical property measurements from Oxford University and University of California – Berkeley. The findings of this comparison were included in previous reports and the major accomplishments are included in a later section.

Multiple ion beam irradiations were performed at the Michigan Ion Beam Laboratory following the successful benchmarking and validation of the enhanced facility. Dual ion irradiations using iron ions and helium ions were performed on two austenitic alloys (800H, Fe21Cr32Ni) and two ferritic-martensitic alloys (T91, HT9) with up to nine different temperatures at ~17 dpa and ~35 dpa to compare directly to the BOR-60 irradiated material to determine the capacity to simulate the in-reactor microstructure. The evolution of the microstructure across this temperature range provided valuable information for modeling the overall microstructure under irradiation. Comparison to the single ion irradiations at similar temperatures demonstrated the strong role helium played in the development of cavities in the microstructure for both core alloy systems as characterized by Pennsylvania State University, University of Michigan, and North Carolina State University. Continued dual ion irradiation to higher dose demonstrated the ability to reproduce the in-reactor microstructure in discrete irradiations steps instead of continual experiments using tailored conditions. The success of the emulation of BOR-60 irradiated microstructures with dual ion irradiation is discussed in a later section.

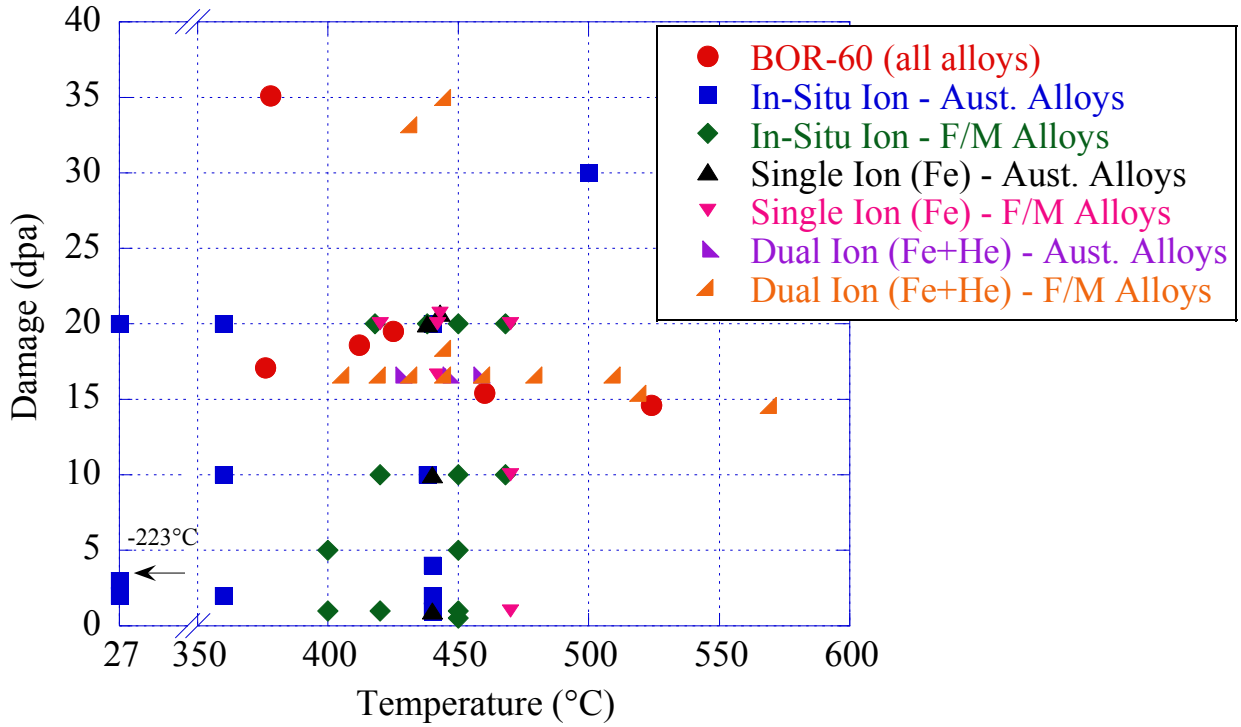

Figure 1.4. Depiction of all irradiation conditions from BOR-60, in-situ ion irradiations, single bulk ion irradiations, and dual ion bulk irradiations examined as part of this project for austenitic alloys and ferritic-martensitic alloys.

2a. Thrust 2a: Microstructure Characterization of Unirradiated and Irradiated Alloys

2a.1. Alloys 800H and Fe-21Cr32Ni

2a.1.1 Microstructure evolution in irradiated alloy 800H (Chris Ulmer and Arthur Motta, Penn State University, Elaina Reese and Emmanuelle A Marquis, University of Michigan)

Major accomplishments of microstructure characterization of irradiated 800H and Fe-21Cr32Ni

1. The irradiation induced features formed on ion irradiated and neutron irradiated alloy 800H after 10-20 dpa were similar. These included both 111 and 110 type loops, irradiation induced segregation and formation of voids.
2. Using the appropriate temperature shift the loop microstructure was qualitatively and quantitatively reproduced using ion irradiation to a dose of ~ 20 dpa.

One of the primary goals of this project is to simulate neutron irradiation using ion irradiation. The interest in alloy 800H comes from its possible use in next generation and advanced light water reactors. Accordingly, this alloy was irradiated using bulk ion irradiation (single and dual beam), in-situ ion irradiation and using neutron irradiation, the latter being done at the BOR-60 reactor in Russia. The bulk single ion irradiations were done using 5 MeV Fe^{2+} ions to 1, 10 and 20 dpa at 440 °C, the in-situ ion irradiations done with 1 MeV Kr ions at various temperatures, the dual beam irradiations were done to 16.6 dpa with simultaneously added 1 appm He, while the BOR-60 irradiations went to 17.1 and 35.1 dpa at nominally 376 and 378 °C respectively. The irradiated microstructures were carefully characterized and compared to evaluate the feasibility of using ion irradiation as a surrogate for neutron irradiation. We compare three different irradiations: the single beam ion irradiation (SB) to 20 dpa, the dual beam ion irradiation (DB) to 16.6 dpa, and the BOR-60 neutron irradiation to 17.1 dpa. The DB irradiation was carried out using a temperature shift from the neutron irradiation to compensate for the increased dose rate under ion irradiation, and the simultaneous He implantation was performed to simulate transmutation effects in a reactor that are normally absent during ion irradiation.

The most prominent visible microstructural features, were faulted dislocation loops, cavities, irradiation induced segregation to grain boundaries, and precipitates. These were all characterized, as in Figures 2a.1.1 – 2a.1.4. A direct comparison and summary of these results, shown by the ratio of ion irradiation measurement to neutron irradiation measurement, is provided in Figure 5. With the exception of the cavity populations and the behavior of Al at grain boundaries (which depleted during ion irradiation but enriched at grain boundaries during neutron irradiation), the microstructures produced by DB ion irradiation and neutron irradiation share many of the same features and agree, on at least an order of magnitude basis. The cavities formed showed a significant difference: during DB ion irradiation a high density of small, bubble-like features were produced, in contrast to the fewer, larger cavities produced during neutron irradiation.

The results suggest that the temperature shift used for this work was sufficient to produce a similar microstructure for many of the features, indicating that to the dose levels studied ion irradiation may be an effective way to study neutron irradiation given the temperature shift used.

Many of the differences in microstructure, where neutron irradiation generally produced a coarser microstructure than ion irradiation, indicate that a larger temperature shift for ion irradiation could better simulate the microstructure produced during neutron irradiation. The high density of bubble-like cavities formed during DB ion irradiation could be caused by over-nucleation, such that a lower ratio of He implantation to damage could improve the match. This is supported by the SB ion irradiation results, also shown for cavities in Figure 2a.1.5, that show a cavity population that is more similar to that formed under neutron irradiation than that formed during dual beam irradiation.

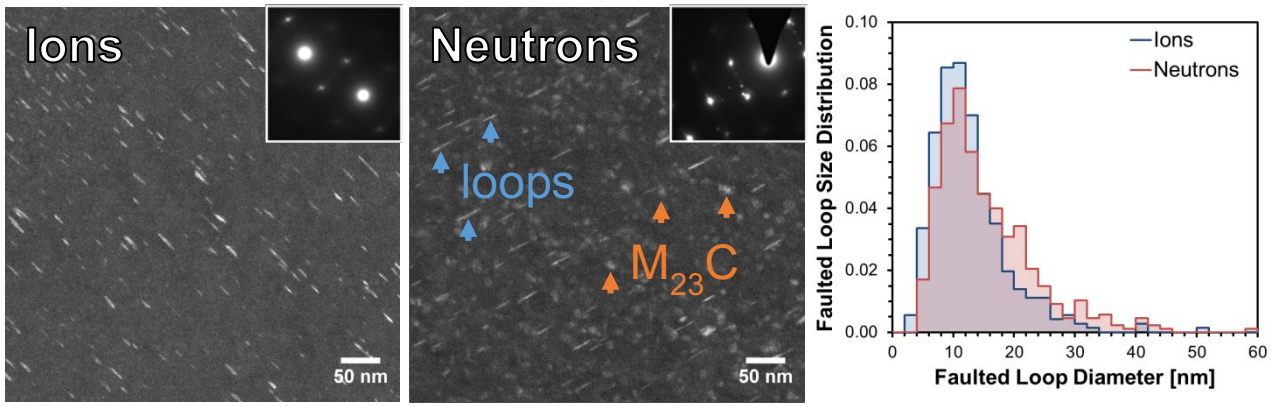

Figure 2a.1.1. Rel-rod dark-field TEM images showing the faulted dislocation loop microstructure after DB ion irradiation to 16.6 dpa and neutron irradiation to 17.1 dpa. Neutron irradiation produced a coarser microstructure with only about one third the density of loops as compared to DB ion irradiation.

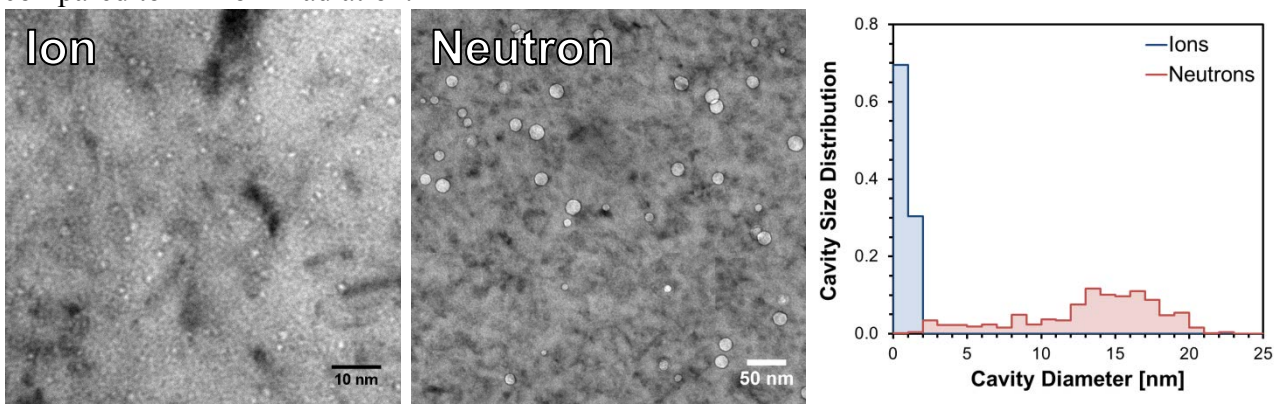

Figure 2a.1.2. Under-focused bright-field TEM images showing the cavity population after DB ion irradiation to 16.6 dpa and neutron irradiation to 17.1 dpa. DB ion irradiation produced a high density of small, bubble-like features while neutron irradiation resulted in 100 to 1000 times fewer cavities but with much larger sizes.

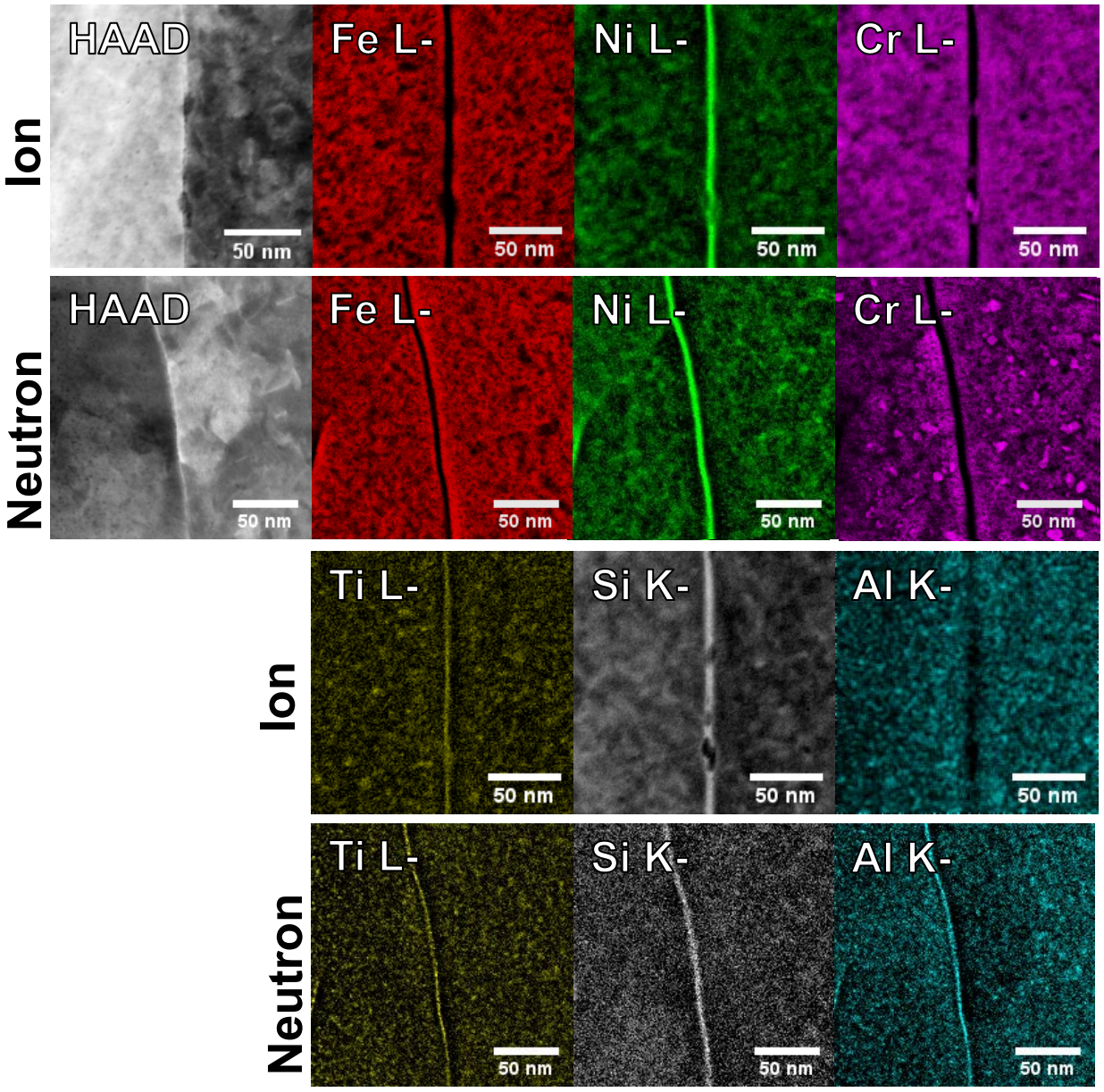

Figure 2a.1.3. Electron energy loss spectroscopy images showing radiation induced/enhanced segregation at grain boundaries after DB ion irradiation to 16.6 dpa and neutron irradiation to 17.1 dpa. Ni, Ti, and Si were enriched for both irradiations, while Fe and Cr were depleted for both irradiations. Al, however, was depleted during ion irradiation and enriched during neutron irradiation.

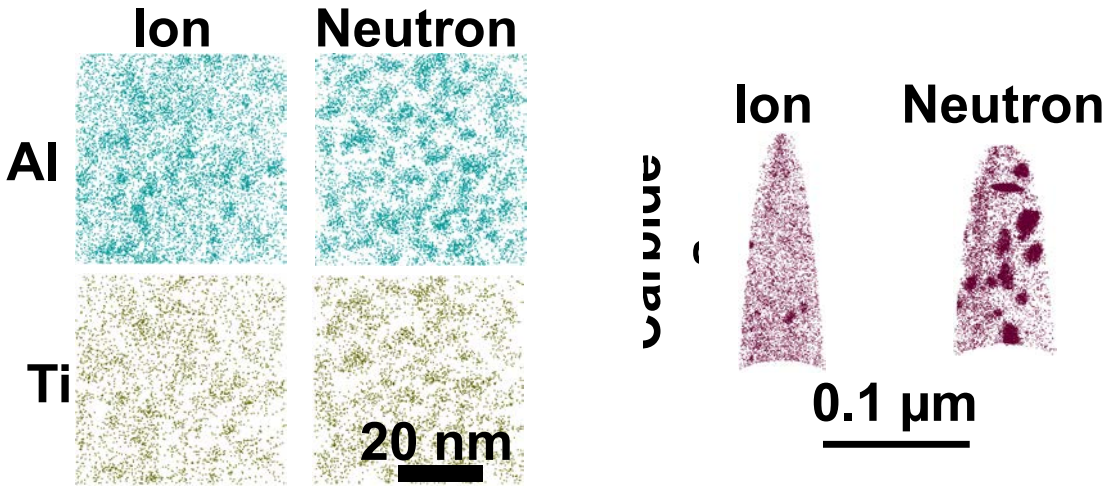

Figure 2a.1.4. Atom probe tomography visualizations showing the presence of Al,Ti-rich clusters and carbides after both DB ion irradiation to 16.6 dpa and neutron irradiation to 17.1 dpa. The most significant differences manifest as a higher density of Al,Ti-rich clusters and a population of larger carbides resulting from neutron irradiation.

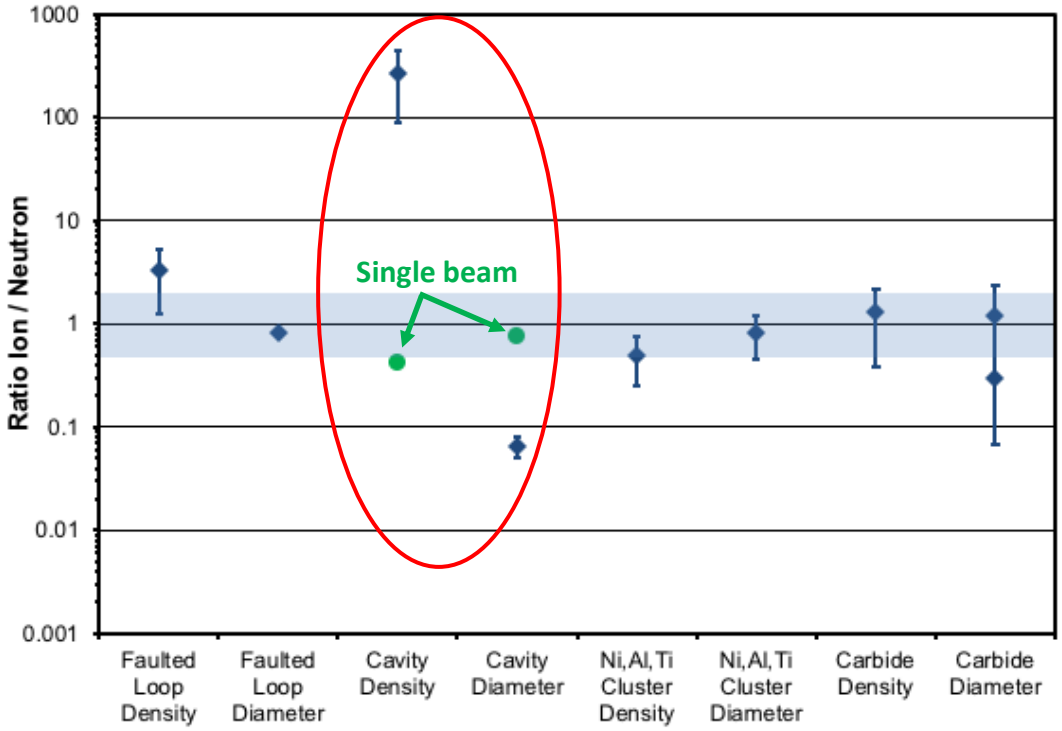

Figure 2a.1.5. Comparison of dual beam ion irradiation to neutron irradiation by showing ratios of measured parameters. The shaded band shows the region where the microstructure agrees by a factor of two. Data points from single beam ion irradiation are provided in green for cavities and show better agreement than for dual beam ion irradiation.

A high temperature and creep resistant Alloy 800H, which is used widely in industry, was subjected to ion irradiation at 440°C using 5 MeV Fe^{2+} ions and neutron irradiation at 385 °C to a dose of 17 dpa. The shallowness of the damaged region created by the heavy ions represents a challenge for the interpretation of the microstructures that can be affected by the proximity of the surface and the implanted interstitial region. Rather than following all previous works traditionally focusing on the microstructure located at an intermediate depth or about 0.5 to 0.6 µm for implantations conducted using 5 MeV Fe^{++} ions, this work reveals the microstructure of Alloy 800H along the heavy ion damage profile and compares them with neutron irradiated samples when possible., Fig. 2a.1.6 The observed microstructural features include spherical Ni, Al, and Ti rich solute clusters consistent with the irradiation-assisted formation of the γ' phase, Ni and Si segregation to dislocation loops, Cr-Ti-rich carbides, and cavities with additional Ni and Si interfacial segregation. Carbides were most abundant and largest around the damage peak, coinciding with lowest densities of dislocation loops and Ni, Al, and Ti rich solute clusters. In the neutron irradiated sample, comparable carbide density and size and Ni, Ti, Al clusters were observed to those found at the ion peak damage.

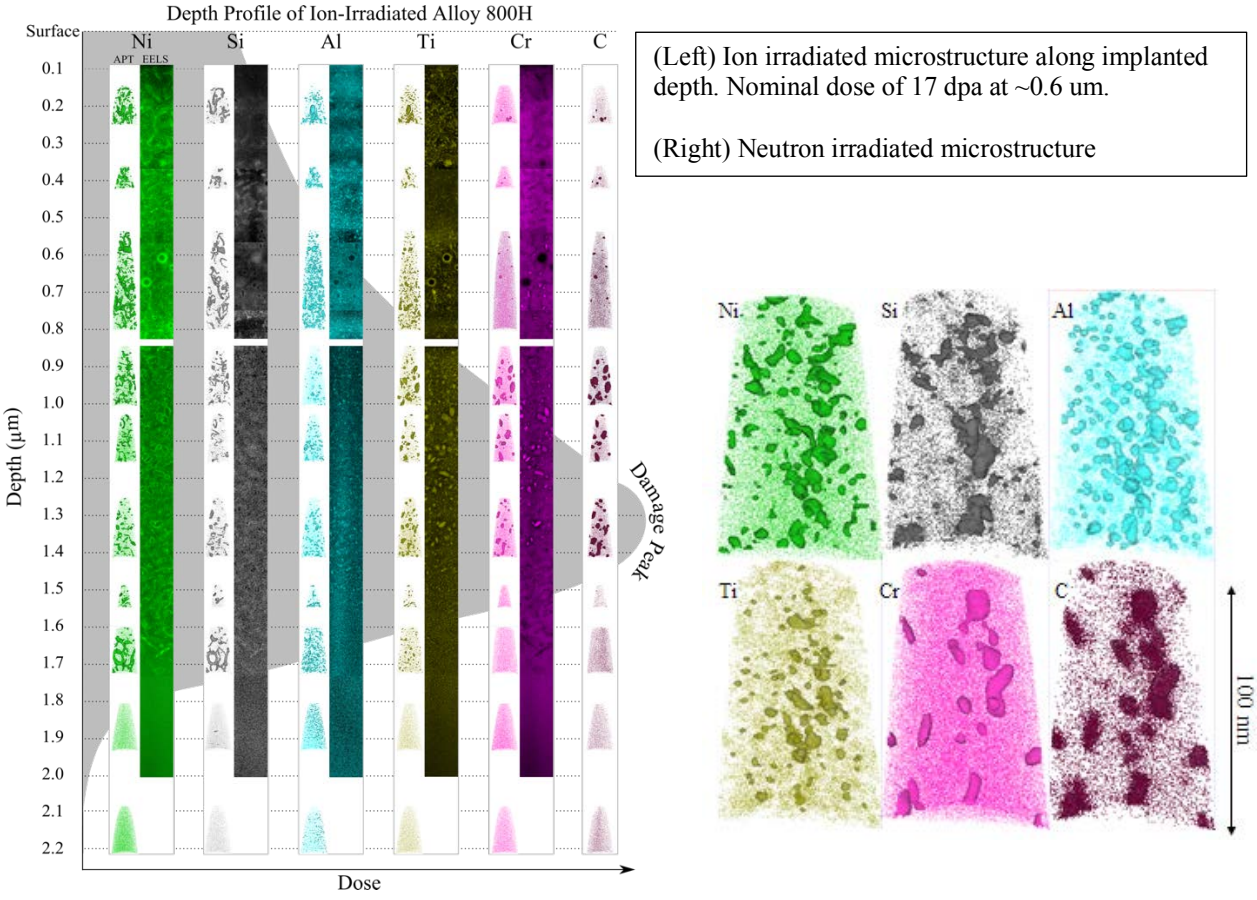

Figure 2a.1.6. Depth profile of composition of ion irradiated alloy 800H to 17 dpa at 440°C.

2a.1.2 Ion irradiation of Fe-21Cr-32Ni model alloy (Chris Ulmer and Arthur Motta, Penn State University, Elaina Reese and Emmanuelle A Marquis, University of Michigan)

Major accomplishments of the microstructure characterization of irradiated Model alloy Fe-21Cr-32Ni

1. The irradiation induced features seen after ion irradiation to ~ 20 dpa of the Model Alloy were quite similar to the sister commercial alloy 800H, in terms of faulted loop density and diameter. Also, the unfaulting mechanism identified was operational in both alloys, leading to the formation of a dense dislocation network.
2. The irradiation induced grain boundary segregation was observed to be qualitatively the same in ion irradiated Model alloy as in 800H.
3. Voids were observed in the ion irradiated microstructures of both alloys, showing lower levels than those under neutron irradiation.

To help understand the irradiation behavior of alloy 800H in greater depth the model alloy 21Cr32Ni was also ion irradiated in a similar manner. Alloys obtained from University of Michigan were irradiated at 440ºC with 5 MeV Fe ions to 1, 10 and 20 dpa in a region 0.6 micron from the outer surface and dual beam irradiated (Fe and He ions) at 446ºC to 16.6 dpa with helium implantation of 1 appm/dpa. The resulting irradiated microstructures were characterized in detail to determine the most important microstructure parameters.

The principal findings are:
(a) Ion irradiation causes dislocation loops to form which grow and eventually coalesce into dislocation networks. The habit planes of the loops formed were both {110} and {111}. Because the latter loops were faulted, they could be imaged using a rel-rod dark field technique in TEM. Voids were also occasionally seen after irradiation.
(b) The faulted loop diameter increased with dose to a maximum of 13-14 nm and saturated between 10 and 20 dpa the loop density. This is thought to be due in part to loop unfaulting, which makes those loops invisible to the imaging technique used in the characterization.
(c) These loops are thought to be interstitial type and their evolution was similar to that seen after irradiation of alloy 800 H. In-situ irradiation experiments show that the faulted loops become unfaulted during the irradiation as shown in Figure 2a.1.7**,** occurring by the glide of another dislocation nearby during the irradiation.

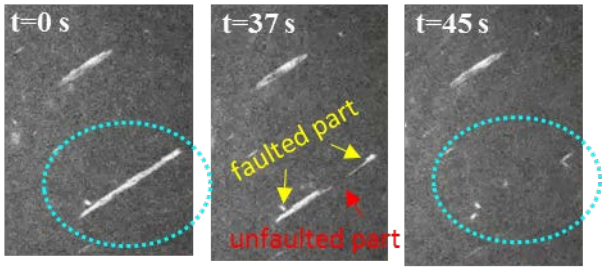

Figure 2a.1.7. Rel-rod dark field images showing the dislocation loop unfaulting during the in-situ irradiation.

(d) Voids were formed in both single beam and dual beam bulk ion irradiation but not during thin foil in situ irradiation (see (e)). The threshold dose for void formation is lower in 21Cr32 Ni

model alloy than for alloy 800H. Void formation was enhanced by dual beam irradiation, as expected. Also voids formed preferentially on dislocations and grain boundaries.
(e) Voids were found to be are unstable during thin foil irradiation. Samples prepared from bulk irradiated material in which voids formed were further irradiated at the IVEM facility at different temperatures. The voids were seen to shrink during irradiation. The calculated shrinkage rates are independent of irradiation temperature, even down to 50 K.

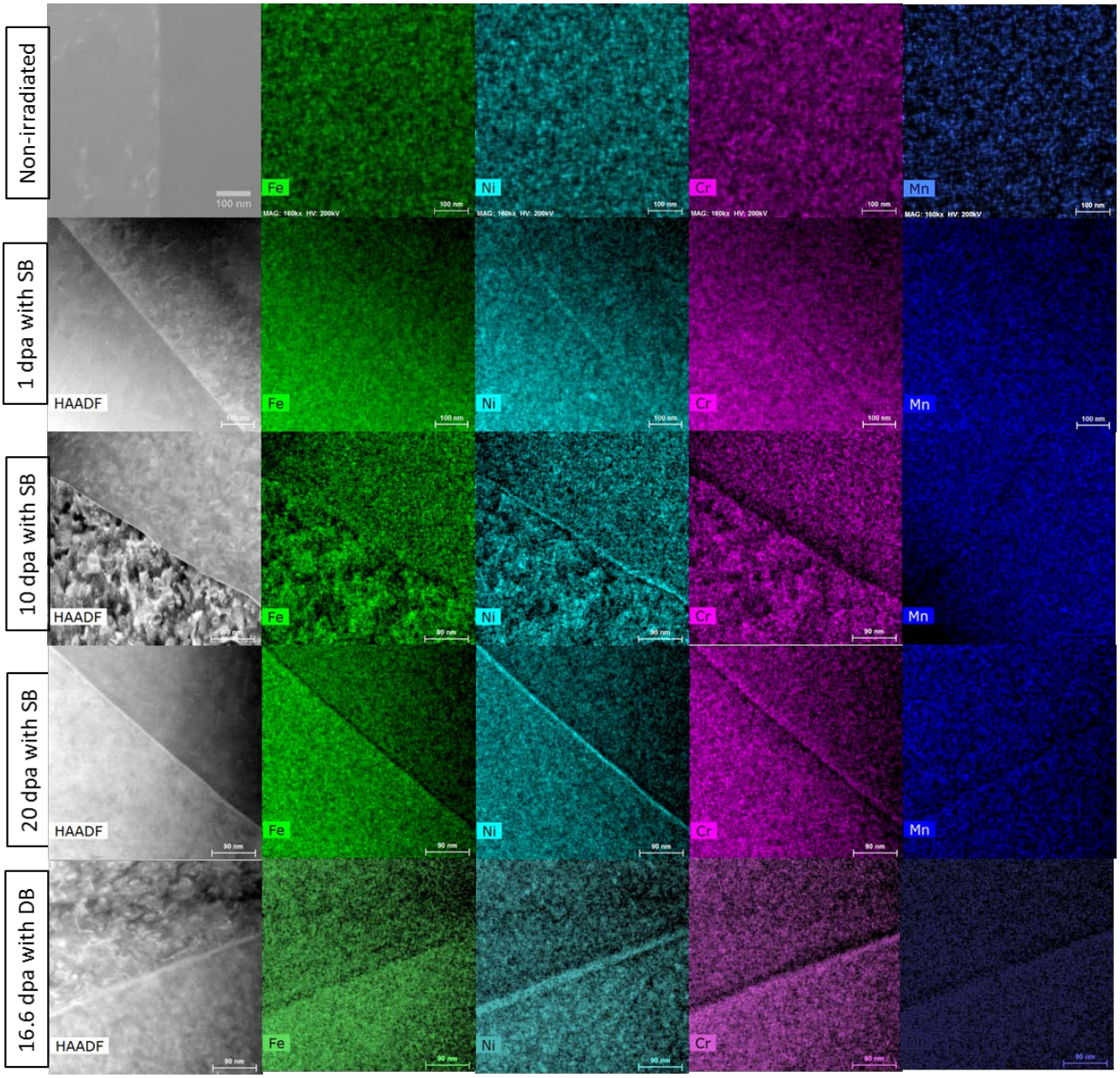

Figure 2a.1.8. Irradiation induced segregation of alloying elements indicated for various doses during bulk irradiation of 21Cr32Ni model alloy. Scale bar (non-irradiated and 1 dpa): 100nm, Scale bar (10, 20 and 16.6 dpa): 90 nm

(f) Irradiation of the 21Cr32Ni model alloy also causes micro-chemical evolution. Chemical mapping of the bulk irradiated alloys collected from the region close to the grain boundary show

Ni segregation with Fe and Cr depletion. The degree of Ni segregation and Fe, Cr and Mn depletion increased with irradiation dose (see Figure 2a.1.8).

(g) Irradiation induced segregation was only observed after irradiation at high temperature: Ni is segregated to the grain boundary while Fe, Cr and Mn show depletion (Fig. 2a.1.9).

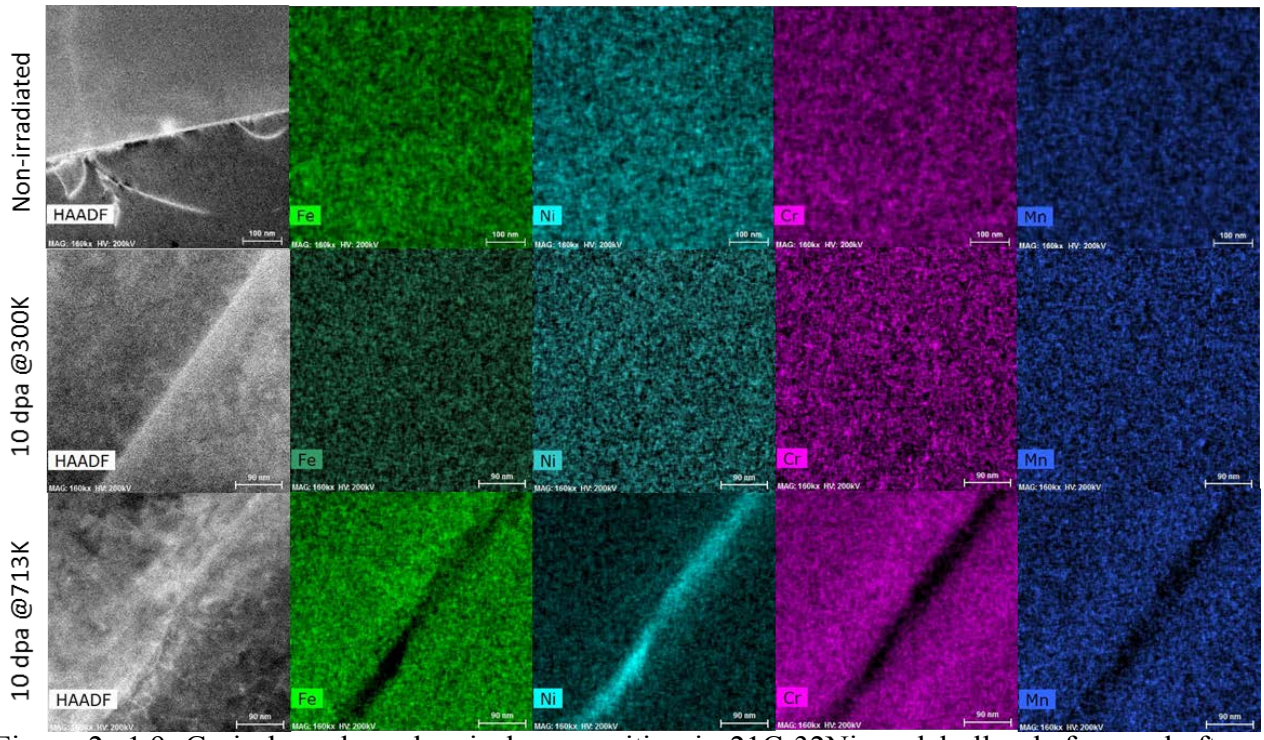

Figure 2a.1.9. Grain boundary chemical composition in 21Cr32Ni model alloy before and after irradiation to 10 dpa with 1 MeV Kr^{++} ions at 300K and 713K, respectively. Scale bar (non-irradiated): 100nm, (irradiated): 90 nm.

2a.1.3 *Comparison of the irradiated microstructure of 21Cr32Ni vs. 800H (Chris Ulmer and Arthur Motta, Penn State University, Elaina Reese and Emmanuelle A Marquis, University of Michigan)*

The model ternary alloy Fe-21Cr-32Ni was irradiated for comparison to its commercial equivalent, alloy 800H, with the idea that its simpler composition and microstructure helps to understand and model the microstructural evolution of the latter. We compare the ion irradiation response of these two alloys.

Non-irradiated microstructure

The microstructure of both alloys before irradiation is similar with a larger grain size for 800H. X-ray diffraction shows that for both 21Cr32Ni model alloy and 800H austenite is the primary phase for both alloys. However, unlike 800H, the 21Cr32Ni model alloy does not include the minor peaks associated with carbide precipitates ($M_{23}C_6$ and MC-type) which were also observed in 2132 with TEM microscopy. Electron Back Scattered Diffraction (EBSD) images showed no obvious preferential grain orientation of for either alloy. Although similar heat treatments were

applied, the average grain size was calculated as ~60 nm for 21Cr32Ni model alloy which is about a factor of 3 than the average grain size for 800H.

Irradiated microstructure
TEM characterization of the bulk irradiated alloys shows that both alloys exhibit dislocation loops after 1 dpa Fe ion irradiation and both dislocation loops and a well-developed dislocation network structure after higher dose irradiations to 10, 16.6 and 20 dpa. The loops observed in the 21Cr32Ni model alloy show both {111} and {110} type habit planes while only the {111} type habit plane was observed in 800H.

The average faulted loop diameter measured for the 21Cr32Ni model alloy was found to be very similar to those measured for 800H for each irradiation condition as shown in Fig. 2a.1.10a. The number density of faulted loops also shows similar behavior and increases with increasing dose. The loop density is, however, found to be higher in 800H compared to that of the model alloy (by a factor of ~2-3 in single beam ion irradiation).

The cavity behavior in single beam irradiated 21Cr32Ni model alloy and 800H shows notable differences. While voids formed after 1 dpa single beam irradiation of 21Cr32Ni, no voids were observed after irradiation of 800H to that dose. At higher doses of 10 and 20 dpa, voids form ion both alloys formation but show differences in their distribution. While the voids observed in 10 and 20 dpa single beam irradiated 800H are uniformly distributed within the ion range (100-1000nm) in the 21Cr32Ni model alloy, at that dose voids were only observed deeper into the alloys, about 1400-2000nm depth from the irradiated surface.

Dual beam irradiation of the both allots 16.6 dpa and 16.6 appm He results in much smaller and more numerous cavities than in single beam irradiation indicating that the helium implantation promotes cavity nucleation in both alloys. The cavity distributions observed after dual beam irradiation of both 21Cr32Ni and 800H alloys are similar, in that they were observed mostly within the ion range, but not near the outer the surface (<~200-300nm) or the ion implanted region (>~1000-1200nm). Cavities were larger in 2132 than in 800H: the measured average cavity diameters were 1.9 ± 0.3 nm for 21Cr32Ni model alloy and and 0.9 ± 0.1 nm for 800H. The corresponding cavity number density was higher for 800H: $(35 \pm 10)\times10^{22}$ m^{-3},in 800 H versus $(7.9 \pm 1.9)\times10^{22}$ m^{-3} in 2132. The smaller cavities (factor of ~2) with higher density (factor of ~4.5) in 800H suggests that alloying elements may help promote void nucleation during dual beam irradiation in that alloy. In both alloys voids were found to be unstable during think foil irradiation, and voids previously formed during bulk irradiation shrank and disappeared under subsequent thin foil irradiation at a range of temperatures.

Irradiation of the 21Cr32Ni model alloy and 800H results in similar chemical evolution along the grain boundaries. Energy Dispersive X-ray spectrum (EDX) analysis performed for 800H shows Ni segregation with Fe and Cr depletion along the grain boundaries similar to what was observed in the irradiated 21Cr32Ni model alloy. In the 21Cr32Ni model alloy, in addition to Fe and Cr depletion, Mn was also observed to be depleted.

While segregation of the major alloying elements to grain boundaries was similar in both alloys, that of major and minor alloying elements to matrix features was not. Ni segregation along with

Fe and Cr depletion were observed in the vicinity of defects such as dislocations and cavities in both alloys. No such segregation was detected in the matrix of either 800H or 21Cr32Ni model alloy irradiated to 1 dpa. On the other hand, irradiation of 800H to 10 and 20 dpa results in homogenously distributed Si, Ni-rich loops, Al, Ti-rich features and Cr, Ti-rich carbides in the matrix while no similar distinguishable irradiation precipitates or features were detected in the matrix of 21Cr32Ni model alloy after irradiation. This suggests that the segregation of additional elements to irradiation induced defects plays a role in microstructure evolution of 800 H but not in the model alloy.

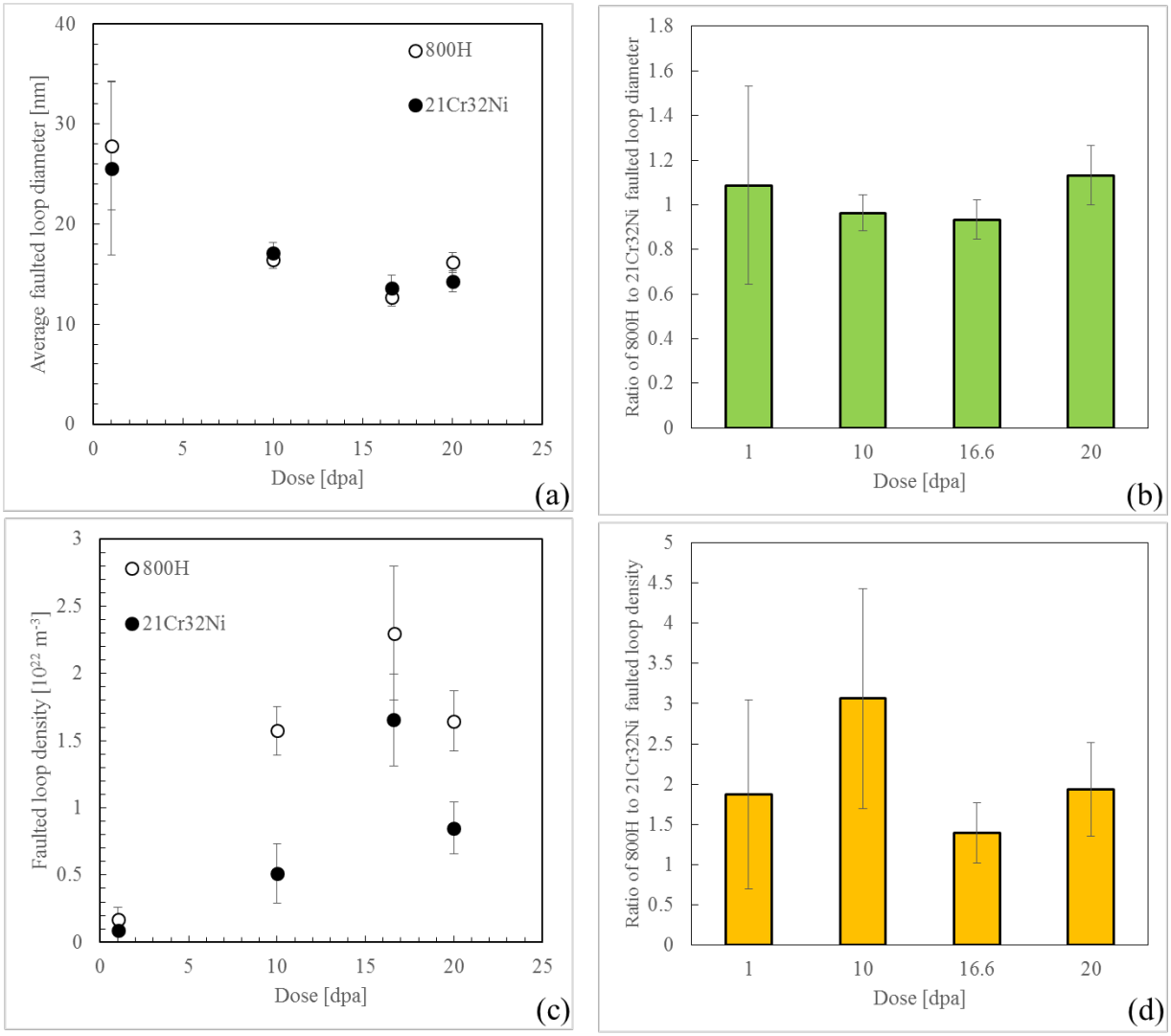

Figure 2a.1.10 Comparison of (a-b) average faulted loop diameter vs. dose, (c-d) faulted loop density vs. dose in 21Cr32Ni model alloy and 800H.

2a.2. Alloys T91 and HT9

Alloy T91

2a.2.1. BOR-60 Irradiated T91 (U. of Michigan, Taller and Jiao, ORNL, Field, U. of Oxford, Yeli)

Microstructures (dislocation loops, cavities and radiation-induced precipitates) and grain boundary microchemistry (radiation-induced segregation) of T91 neutron irradiated in the BOR60 reactor at five temperatures between 376°C and 524°C to doses between 15.4 and 35.1 dpa were characterized using transmission electron microscopy (TEM), scanning transmission electron microscopy (STEM), and atom probe tomography (APT). The characterization results are given in Table 2a.2.1 and Table 2a.2.2 x. The major observations/findings are as follows.

Table 2a.2.1. Summary of characterization results for Ni/Si-rich precipitates, cavities and dislocation loops in T91 irradiated at various conditions in BOR60. Error in sizes is the larger of the standard error of the mean and pixel resolution of the image. Error in number densities (not shown) is due to TEM foil thickness measurement and is estimated to be 10%.

		Ni/Si-rich precipitates			Cavities				Dislocation loops		
T (° C)	Dose (dpa)	Average size (nm)	Number density (10^{21} m^{-3})	Vol. fraction (%)	Average void size (nm) (cavities > 2 nm)	Number density of void (10^{20} m^{-3}) (cavities > 2 nm)	Number density of bubbles (10^{20} m^{-3}) (cavities < 2 nm)	Void swelling (%)	Average diameter (nm)	Number density (10^{21} m^{-3})	Dislocation loop line density (10^{14} m^{-2})
376	17.1	5.8±0.5	3.6	0.037	6.9±1.1	7.3	1200	0.016	21.8±0.5	2.9	2.0
378	35.1	7.0±0.5	2.4	0.043	6.5±1.1	14.7	220	0.033	22.9±1.2	1.9	1.4
415	18.6	6.7±0.5	3.0	0.047	5.6±1.1	6.5	160	0.0058	25.8±0.9	2.0	1.9
460	14.6	N.O.	N.O.	N.O.	N.O.	N.O.	32	Negl.	Negl.	Negl.	Negl.
524	15.4	N.O.	N.O.	N.O.	N.O.	N.O.	33	0	N.O.	N.O.	N.O.

Table 2a.2.2. Summary of Cr, Ni and Si grain boundary concentrations and changes from nominal in T91 irradiated in BOR60.

T (°C)	Dose (dpa)	Cr	ΔCr	Ni	ΔNi	Si	ΔSi
376	17.1	9.7±0.2	2.8	1.4±0.3	1.0	1.0±0.3	0.5
378	35.1	9.0±0.2	2.4	1.3±0.3	0.9	1.0±0.3	0.6
415	18.6	12.0±0.2	5.5	1.6±0.3	1.3	1.4±0.3	0.9
460	14.6	12.5±0.2	6.1	1.3±0.3	0.9	0.8±0.3	0.4
524	15.4	9.5±0.2	3.2	0.6±0.3	0.2	0.6±0.3	0.2

1. **Dislocation loops were observed at 376°C-415°C while only network dislocations were observed at 460°C and 524°C. The dominance of network dislocations at high temperatures of 460°C and 524°C is consistent with observations of F-M alloys in FFTF irradiations. Dislocation loops saturated at 17.1 dpa at 376°C. Dislocation loops were mainly a<100> type in BOR60 irradiated T91 which is also consistent with observations in FFTF irradiation.**

STEM-BF images of dislocation loops under different BOR60 irradiation conditions are shown in Figure 2a.2.1a-c and a summary of the average dislocation loop diameter and number density is given in Table 2a.2.1. Images of dislocation loops for BOR60 irradiated T91 at 376°C:17.1dpa and 378°C:35.1dpa are shown in Figure 2a.2.1a and Figure 2a.2.1b, respectively. Both images were taken near the <100> zone axis and thus loops with a Burgers vector of a<100> on (010) and (001) planes appeared as nearly edge-on in the images as indicated by arrows. Both irradiation conditions show the dominance of a<100> loops compared to loops with Burgers vector a/2<111>. This is consistent with the observations by Katoh et al. [1] who observed only a<100> dislocation loops in Fe-Cr binary ferritic alloys irradiated to 140 dpa at 425°C in the Materials Open Test Assembly in the Fast Flux Test Facility (FFTF). Sencer et al. [2] also confirmed the prevalence of a<100> loops in HT9 irradiated to 150 dpa at 443°C. The observations of the nature of loops in BOR60 appeared to be consistent with those in FFTF irradiated in a similar temperature range. The loop size distributions for these two irradiation doses are shown in Figure 2a.2.1f. The slight increase in average loop diameter and decrease in number density at 35.1 dpa were mainly due to the absence of smaller loops (<10 nm) in this condition, although the number density appeared to drop in nearly all the loop size bins. Besides a<100> loops, a possible 1/2a<111> loop that did not show up as edge-on in the image and did not align with other a<100> loops is circled in Figure 2a.2.1a. The density of 1/2a<111> loops was estimated to be less than 10% of the a<100> loop density.

Figure 2a.2.1c shows dislocation loops in T91 irradiated at 415°C:18.6 dpa. The average loop diameter increased and the number density decreased compared to the lower temperature irradiation (376°C:17.1 dpa), as indicated by a shift in the loop size distribution shifted to larger loop size (Figure 2a.2.1f). Figure 2a.2.1d and Figure 2a.2.1e show dislocation images in T91 irradiated at 460°C:14.6 dpa, and at 524°C:15.4 dpa, respectively. No dislocation loops were identifiable. Network dislocations appeared to be the dominant dislocation microstructure. Henry and Maloy [3] noted that loops were observed up to irradiation temperatures in the range 400–450°C for fast reactors, while at higher temperatures only network dislocations were present. The absence of dislocation loops at 460°C and 524°C in BOR60 irradiated T91 is consistent with their observations. There was significant area-to-area variation in network dislocation density for all irradiation conditions, typically in the range of $\sim 5\times10^{14}$–$\sim 5\times10^{15} m^{-2}$. Irradiation at the examined irradiation conditions did not seem to significantly alter the existing network dislocation density from the as-received condition.

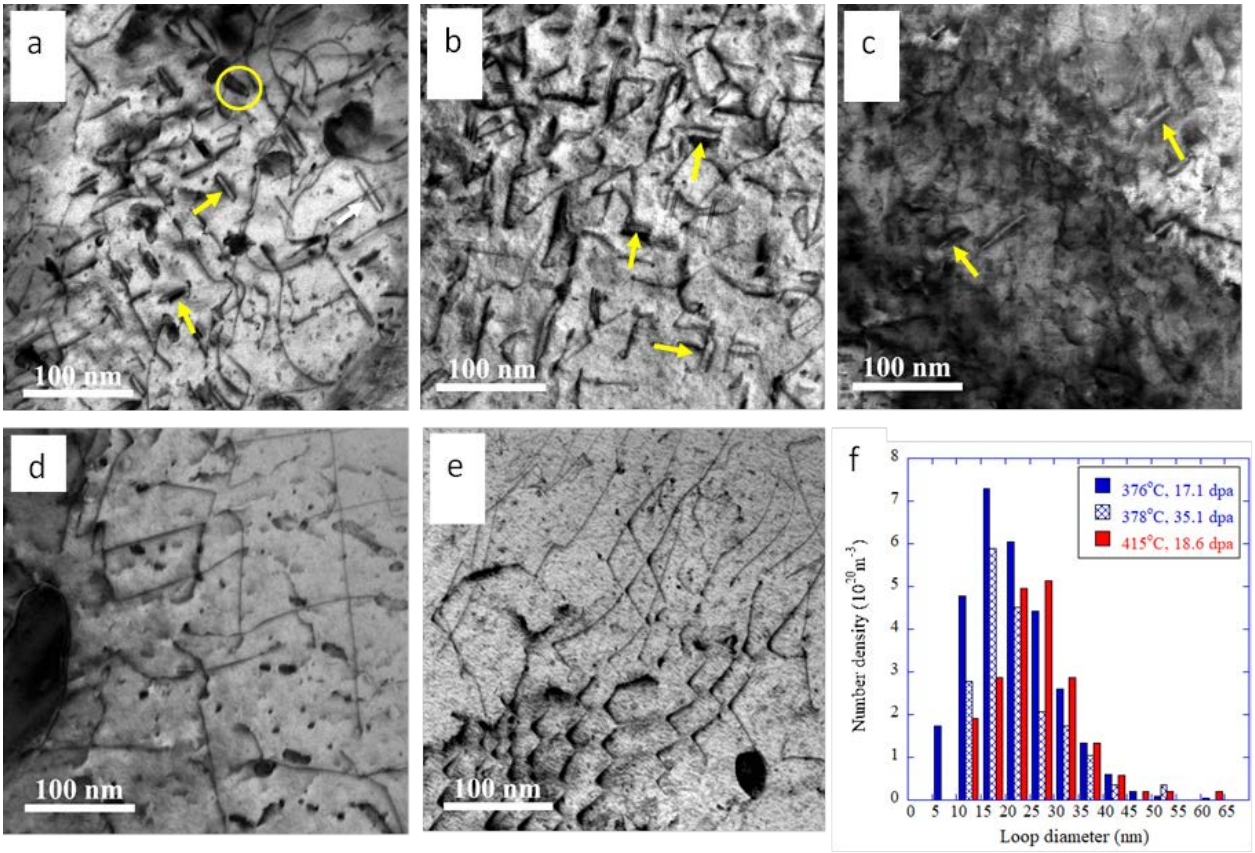

Figure 2a.2.1. STEM-BF images showing dislocation evolution in T91 irradiated in BOR60 under different irradiation conditions: (a) 376°C:17.1dpa; (b) 378°C:35.1dpa; (c) 415°C:18.6 dpa; (d) 460°C:14.6 dpa; and (e) 524°C,15.4 dpa; (f) dislocation size distribution. Some near edge-on dislocation loops are indicated by arrows. A possible 1/2a<111> type dislocation loop is circled in (a)).

1. *Y. Katoh, A. Kohyama, D.S. Gelles, J. Nucl. Mater. 225 (1995) 154-162*
2. *B.H. Sencer, J.R. Kennedy, J.I. Cole, S.A. Maloy, F.A. Garner, J. Nucl. Mater. 414 (2011) 237-242*
3. *J. Henry, S.A. Maloy, in: Pascal Yvon (Ed.), Structural Materials for Generation IV Nuclear Reactors, Woodhead Publishing, 2017, Pages 329–355*

2. **Cavities were observed in BOR60 irradiated T91 at all examined irradiation conditions. A bimodal cavity distribution was observed with a high density of small bubbles less than 2 nm in the temperature range 376-415°C. Only small bubbles were observed at 460°C and 524°C. Voids (cavities > 2 nm) were in the nucleation stage at 17.1 dpa and the number density as well as swelling increased with irradiation dose at 376-378°C.**

STEM-HAADF images of cavities in T91 irradiated in BOR60 under different irradiation conditions are shown in Figure 2a.2.2. Some cavities (dark contrast in the HAADF imaging conditions) are indicated by arrows in Figure 2a.2.2a-2c. The STEM-HAADF technique can effectively reveal cavities greater than 2 nm but smaller cavities can be easily missed due to the weak contrast. Underfocus TEM BF technique is capable of imaging cavities less than 2 nm, although the exact size of cavities cannot be accurately determined without proper simulation tools due to the large amount of under focus, which may exceed 1 μm. The inset in Figure 2a.2.2a shows a high density of small cavities as revealed by underfocus TEM BF technique for the 376°C:17.1dpa irradiation condition. The number density of small cavities (< 2nm, referred to "bubbles") was more than two orders of magnitude higher compared to the larger cavities (> 2 nm, referred to as "voids"). Voids were observed at the 376°C:17.1dpa, 378°C:35.1dpa and 415°C:18.6dpa conditions. Void size and number density as well as the bubble density were smaller at the higher irradiation temperature of 415°C. The presence of a high density of small bubbles resulted in a bimodal cavity distribution as seen in Figure 2a.2.2f. No voids were observed at the 460°C:14.6 dpa condition but small bubbles are observed with a number density of 3.2×10^{21} m^{-3}. Small bubbles with an estimated number density of 3.3×10^{21} m^{-3} were also observed in the 524°C:15.4 dpa condition. Void swelling was 0.016% at 376°C:17.1 dpa and it increased to 0.033% at 378°C:35.1 dpa. Swelling was much lower (0.006%) at 415°C:18.6 dpa.

The average void size did not change but the number density nearly doubled when the irradiation dose increased from 17.1 dpa to 35.1 dpa at 376-378°C , indicating that voids were probably still in the nucleation stage at 17.1 dpa. Bubble density appeared to peak at 17.1 dpa as the density at 35.1 dpa dropped to ~1/5 of that at 17.1 dpa. Nucleation of voids may be due to the growth of some of the existing bubbles at lower dose. The average swelling rate up through 35.1 dpa was ~0.001%/dpa for BOR60 irradiated T91. The same heat of T91 (30176) irradiated in FFTF exhibited void swelling of 1.2-1.6% at 413°C to 184 dpa [1] and 1.9-2.6% at 400°C to 208 dpa [2], resulting in an average swelling rate of ~0.01%/dpa, about one order of magnitude higher than BOR60 irradiation at 17-35 dpa. This indicates that T91 samples irradiated in BOR60 were still in the swelling incubation period and probably far from the steady-state swelling regime, which is expected at these relatively lower doses. The wider size distribution at 35.1 dpa vs. to 17.1 dpa (Figure 2a.2.2) indicates that growth of some voids has occurred between with a doubling of dose.

Swelling is strongly affected by interstitial-biased dislocations while neutral sinks such as grain boundaries, pre-existing precipitates and radiation-induced G-phase particles lower the overall population of interstitials and vacancies by providing recombination sites. Dislocations consist of both the pre-existing dislocation network and dislocation loops formed under irradiation. The density of pre-existing dislocations, $\sim1\times10^{15}$ m^{-2}, did not appear to vary significantly at the examined irradiation conditions. The dislocation loop line density of 1.4-2.0 m^{-2} (Table 2a.2.1) accounted for less than 20% of the total dislocation density. Therefore, the pre-existing dislocations probably dominate the swelling behavior at the examined irradiation doses. It is well-established that the swelling rate is dependent on the dislocation/void sink strength ratio, the Q-value [3]. A low swelling rate is expected when Q>>1 which is the case for T91 in the examined dose range because of the high density of dislocations and low swelling.

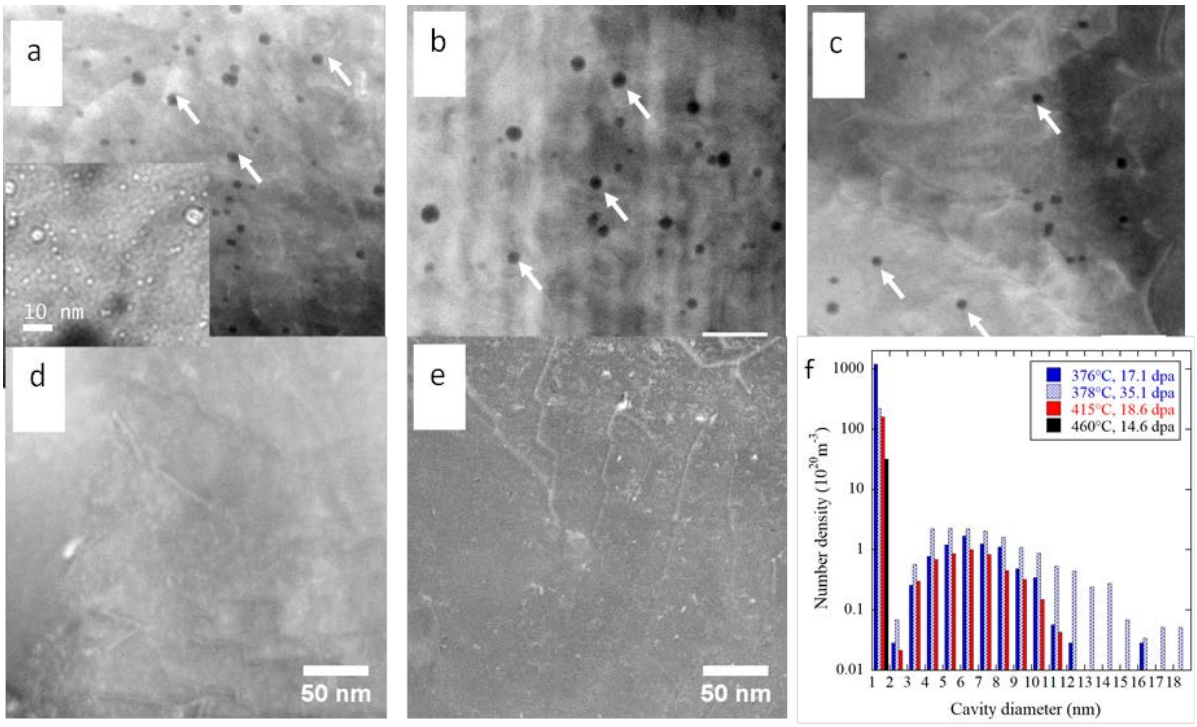

Figure 2a.2.2. STEM HAADF images showing cavity evolution in T91 irradiated in BOR60 under different irradiation conditions: (a) 376°C:17. 1dpa; (b) 378°C:35.1dpa; (c) 415°C:18.6 dpa; (d) 460°C:14.6 dpa; and (e) 524°C:15.4 dpa; (f) size distribution of cavities. Some cavities are indicated by arrows. The inset in (a) is under focus TEM BF images showing high density of small bubbles.

1. *J. Van den Bosch, O. Anderoglu, R. Dickerson, M. Hartl, P. Dickerson, J.A. Aguiar, P. Hosemann, M.B. Toloczko, S.A. Maloy, J. Nucl. Mater. 440 (2013) 91–97*
2. *M.B. Toloczko, F.A. Garner, C.R. Eiholzer, J. Nucl. Mater. 212–215 (1994) 604.*
3. *G.S. Was, Fundamentals of Radiation Materials Science: Metals and Alloys, Second Edition, Springer, Berlin, 2017. p. 418-425.*

3. The dominant radiation-induced precipitates were the Ni/Si-rich G-phase precipitates in BOR60 irradiated T91. The average size and volume fraction increased slightly with dose and temperature but a continued increase in volume fraction was not expected at much higher doses due to the low bulk Ni content. The absence of Ni/Si-rich precipitates at 460°C was likely due to the lack of dislocation loops as additional nucleation sites. No Ni/Si-rich precipitates were observed at 524°C due to the minimal RIS of Ni and Si at the temperature. Cu-rich precipitates were observed in BOR60 irradiated T91 at 376-415°C.

The major radiation-induced precipitates are the Ni/Si-rich precipitates and Cu-rich precipitates. The nature of radiation-induced precipitates was f examined using APT. Figure 2a.2.3 shows the presence of Ni/Si/Mn-rich and Cu-rich precipitates in T91 irradiated at 415°C:18.6 dpa. Ni/Si/Mn-rich clusters are highlighted using iso-concentration surfaces of Mn + Ni + Si at 5 at% in Figure 2a.2.4a and 4c for two different APT tips. Composition proximity histograms of Cluster 1 in Figure 2a.2.4a and Cluster 2 in Figure 2a.2.4c are plotted in Figure 2a.2.4b and Figure 2a.2.4d, respectively. The core region of Cluster 2 contains around 40 at% Ni, 20 at% Si and 10 at% Mn , which is close to the composition G-phase ($Mn_6Ni_{16}Si_7$ with ~21 at% Mn, 55 at% Ni and 24 at% Si). Cluster 1 shows much lower Ni/Si/Mn concentration than that of G-phase. Therefore, judged from compositions, the Ni/Si-rich clusters are likely G-phase or its precursors.

Evolution of the Ni/Si-rich precipitates at different irradiation conditions is shown in Figure 2a.2.5. The distribution of Ni/Si-rich precipitates is shown in Figure 2a.2.5f. The average precipitate size increased slightly from 5.8 nm at 376°C:17.1dpa to 7.0 nm at 378°C:35.1dpa while the number density slightly decreased from 3.6×10^{21} m^{-3} to 2.4×10^{21} m^{-3}. Irradiation at 415°C:18.6 dpa resulted in slightly larger precipitates (6.7 nm) with lower density (3.0×10^{21} m^{-3}) compared to the 376°C:17.1dpa irradiation. A slight increase in size and a decrease in number density with dose indicates that precipitates are still evolving with irradiation at 376-378°C and 35 dpa. However, the volume fractions are nearly the same, ~0.04% at both doses (Table 2a.2.1). The volume fraction did not change significantly at high doses. The theoretical volume fraction of G-phase in T91 assuming that all Ni (~0.1%) is consumed by G-phase is ~0.2%. As Ni and Si also segregate to dislocations, grain boundaries and other interfaces, the maximum volume fraction is expected to be much less that 0.2%. Combined with the saturation of RIS, significant increase in volume fraction of G-phase precipitates at higher doses is not expected, although the precipitate size and density may still evolve with dose. The absence of G-phase at 460°C in BOR60 irradiated T91 was unexpected as significant segregation of Ni and Si still occurred at this temperature (Figure 2a.2.6). Anderoglu et al. [1] reported a few large G-phase precipitates observed at grain boundary triple junctions but not within the grains or laths in FFTF-irradiated HT9 at 466°C to 92 dpa. However, both Ni and Si contents in HT9 are much higher than in T91 (Ni: 0.48 vs. 0.10; Si: 0.41 vs. 0.25 in wt%). The absence of G-phase in T91 at 460°C is, therefore, not unreasonable considering the low bulk Ni and Si contents. As segregation of Ni/Si is minimal at 524°C, formation of G-phase was not expected in BOR60 irradiated T91 at that temperature.

Cu-rich clusters were observed in BOR60 irradiated T91 at 376-415°C. The solubility of Cu in α-Fe is very low (0.003 wt% at ~300°C [2]) and Cu in T91 is likely supersaturated at the BOR60 irradiation temperatures even though the bulk content is only 0.062 wt%. Radiation enhanced formation of Cu-rich clusters was reported in proton irradiated T91 and HCM12A [**Error! Reference source not found.**] and the volume fraction of Cu-rich precipitates was shown to be dependent on bulk Cu content. APT revealed that Cu-rich precipitates were associated with Ni/Si-rich precipitates, dislocations and grain boundaries [3]. Besides the increase in Cu solubility at higher temperatures, the lack of Ni/Si-rich precipitates and dislocation loops at 460°C and 524°C may also contribute the absence of Cu-rich precipitates at these higher temperatures.

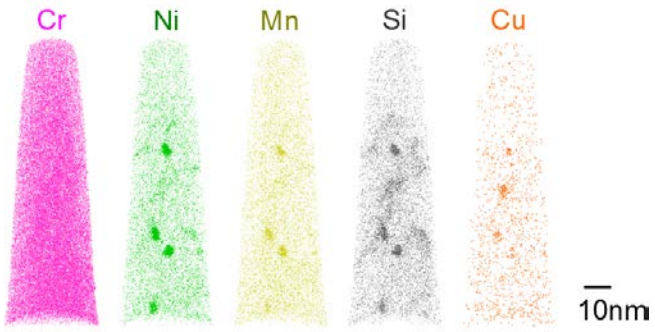

Figure 2a.2.3. Atom maps of T91 irradiated in BOR60 to 415°C:18.6 dpa.

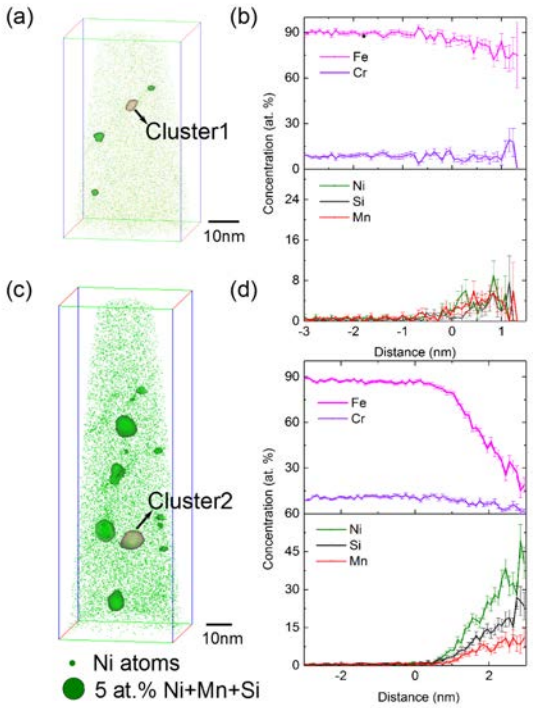

Figure 2a.2.4. (a) (c) Ni/Si/Mn-rich clusters highlighted using iso-concentration surfaces of Mn + Ni + Si at 5 at% in two different APT tips from T91 irradiated in BOR60 to 415°C:18.6 dpa. (b) (d) Proximity histograms showing the concentrations of major elements in Cluster 1 and Cluster 2, respectively.

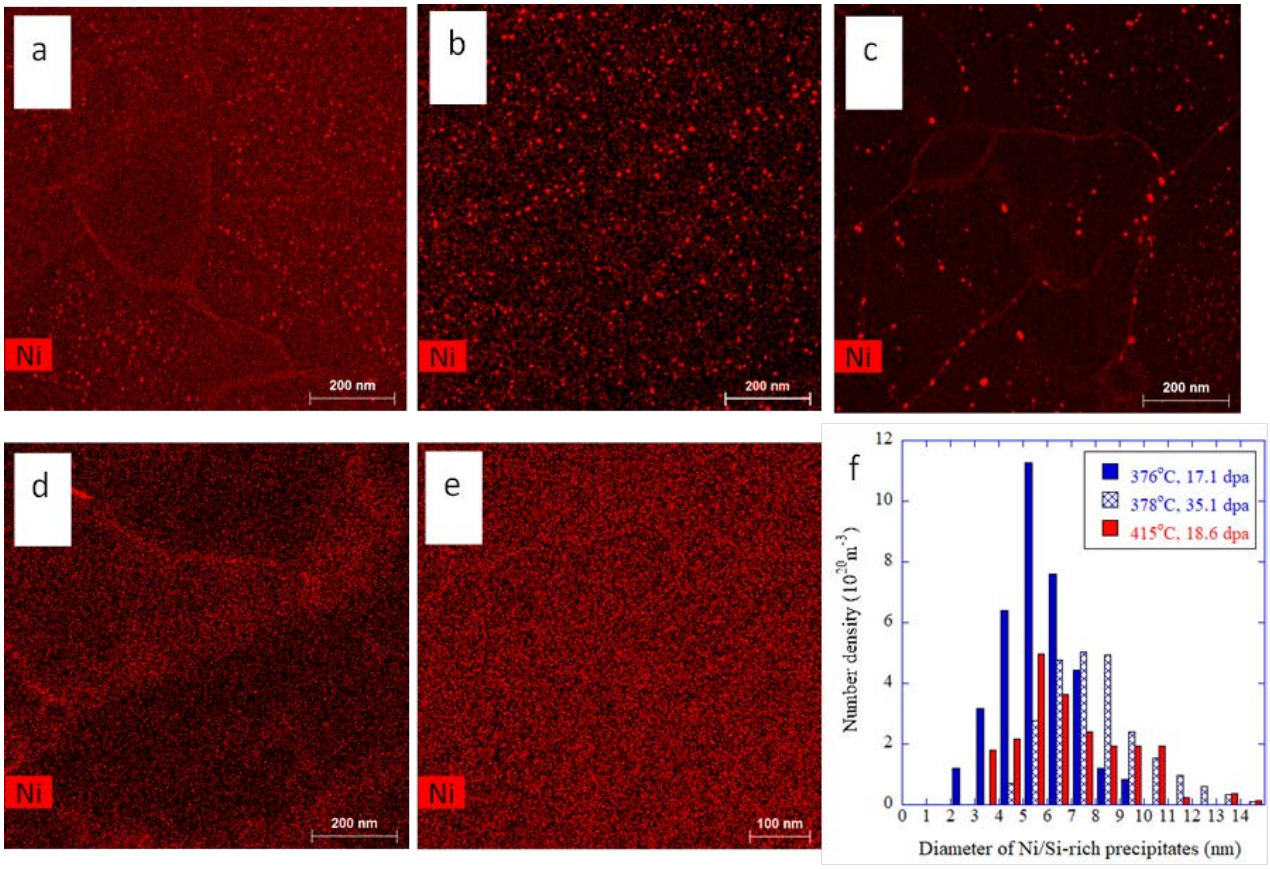

Figure 2a.2.5. Ni/Si-rich clusters or G-phase evolution in T91 irradiated in BOR60 under different irradiation conditions: (a) 376°C:17.1dpa; (b) 378°C:35.1dpa; (c) 415°C:18.6 dpa; (d) 460°:14.6 dpa; and (e) 524°C:15.4 dpa; (f) G-phase size distribution.

1. *O. Anderoglu, J. Van den Bosch, P. Hosemann, E. Stergar, B.H. Sencer, D. Bhattacharyya, R. Dickerson, P. Dickerson, M. Hartl, S.A. Maloy, J. Nucl. Mater. 430 (2012) 194*
2. *G.R. Odette, G.E. Lucas, Radiat. Eff. Defects Solids 144 (1) (1998) 189–231*
3. Z. Jiao, V. Shankar, G.S. Was, J. Nucl. Mater. 419 (2011) 52-62

4. **Enrichment of Cr, Ni and Si at the grain boundary occurred at all doses and temperatures. At a temperature of 376°C RIS appeared to saturate at 17.1 dpa. Cr enrichment peaked at a temperature of 460°C, and Ni and Si enrichments peaked at lower temperatures.**

Composition profiles across the grain boundary for Fe, Cr, Ni and Si for all the irradiation conditions are shown in Figure 2a.2.6. Depletion of Fe and enrichment of Cr, Ni and Si at the grain boundary were evident. Concentrations of Cr, Ni and Si at the grain boundary as well as the magnitude of depletion/enrichment are given in Table 2a.2.2. Iron depleted at all the irradiation conditions with the maximum depletion occurring at 460°C. Enrichment of Cr was observed for all profiles with minimal enrichment of <3 wt% at 376-378°C and maximal enrichment of ~6 wt% at 460°C. Both Ni and Si enriched at the grain boundary but the enrichment was minimal at 524°C (~0.2 wt%). Enrichment of Cr, Ni and Si at the grain boundary as a function of temperature is shown in Figure 2a.2.7. Enrichment of Cr peaked around 460°C while Ni and Si appeared to peak at lower temperature. An increase in the irradiation dose from 17.1 dpa to 35.1 dpa did not appear to affect the magnitude of enrichment for all three elements at 376-378°C (open and closed circle symbols in Figure 2a.2.7).

There was negligible change in the magnitude of enrichment for Cr, Ni and Si at 35.1 dpa compared to 17.1 dpa at 376-378°C, indicating that RIS has saturated by 17 dpa (Figure 2a.2.6). Saturation of RIS occurs when the concentration gradient of the enriched element at the grain boundary rises to the level where backward diffusion balances enrichment by RIS. However, the extent of segregation increases with temperature to a maximum at 460°C. Observed enrichment of Cr, Ni and Si at the grain boundary in BOR60-irradiated T91 is consistent with proton irradiated T91 [1-3] at similar irradiation temperatures. RIS behavior of Cr in F-M alloys can be explained by the diffusion coefficient ratio of Cr to Fe for both vacancies and interstitials [2,3]. Enrichment of Cr occurs at lower temperature when the interstitial diffusion coefficient ratio dominates, and depletion occurs at high temperatures when the vacancy diffusion coefficient ratio dominates. The cross-over temperature appeared to be around 600°C for proton irradiated T91 [3]. The temperature dependence of the diffusivity ratio resulted in a maximum enrichment of Cr at ~450°C for proton-irradiated T91 [3], consistent with the observed temperature dependence of Cr enrichment in BOR60-irradiated T91 of 460°C. Minor elements Ni and Si showed a peak in segregation at a lower temperature of ~400°C, also consistent with proton irradiations [3].

It is noteworthy that while there is significant RIS at 460°C, dislocation loops, Ni/Si-rich precipitates as well as voids larger than 2 nm were all absent. Contrary to RIS that requires only the flow of defects to the sink, voids, loops and precipitates depend on a net flux of one type of defects for nucleation to occur. It appears that the net flux of interstitials or vacancies could not be maintained at a high enough level to counteract thermal emission at the irradiation temperature, so nucleation of dislocation loops and voids did not occur. The lack of nucleation of Ni/Si-rich precipitates at 460°C may be due partially to the lack of dislocation loops as additional nucleation sites besides pre-existing dislocations.

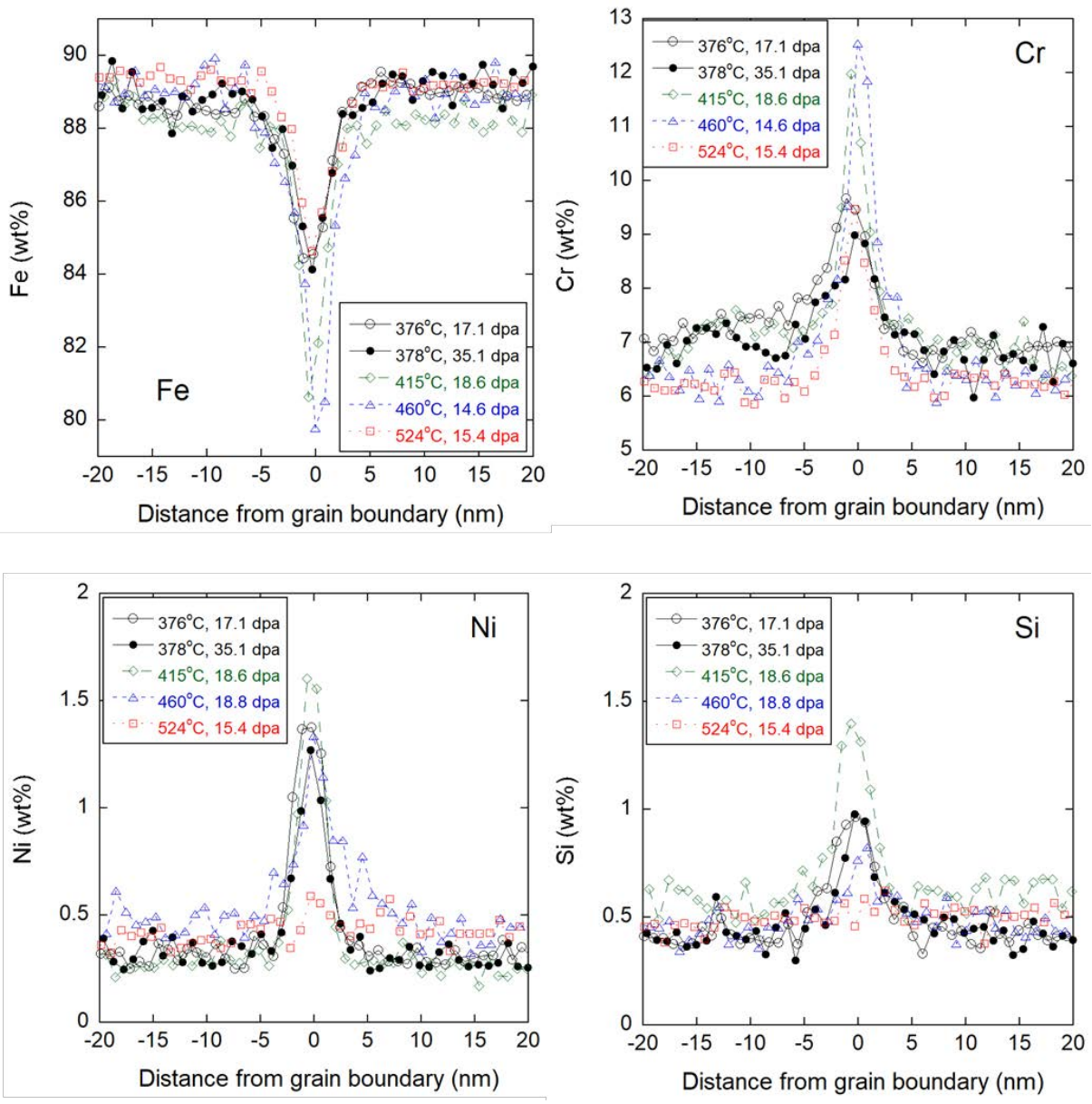

Figure 2a.2.6. Radiation induced segregation profiles of Fe, Cr, Ni and Si across the grain boundary in T91 irradiated in BOR60 under different irradiation conditions.

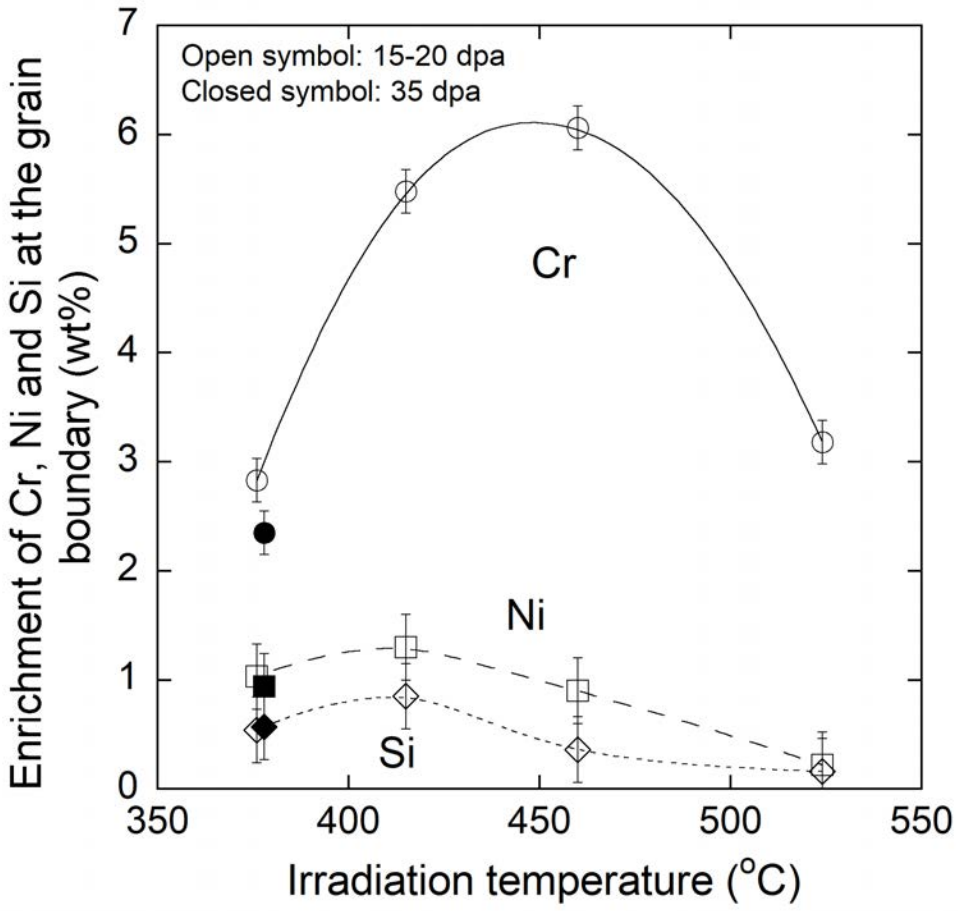

Figure 2a.2.7. Irradiation dose and temperature effect on enrichment of Cr, Ni and Si at the grain boundary in BOR60-irradiated T91.

1. *G. Gupta, Z. Jiao, A.N. Ham, J.T. Busby, G.S. Was, J. Nucl. Mater. 351 (2006) 162-173*
2. *G.S. Was, J.P. Wharry, B. Frisbie, B.D. Wirth, D. Morgan, J.D. Tucker, T.R. Allen, J. Nucl. Mater. 411 (2011) 4*
3. *J.P. Wharry, G.S. Was, Acta Mater. 65 (2014) 42–55.*

2a.2.2. Ion irradiation to emulate BOR60 irradiation in T91 (UM, Taller and Jiao, ORNL, Field)

1. **Helium was found necessary to nucleate cavities at low damage levels using both single ion irradiations with pre-implanted helium and dual ion irradiation with simultaneous co-injection of helium.**

Early in the project, single ion irradiations were conducted on T91 heat 30176 to 20 dpa at 420°C, 440°C, and 470°C with and without room temperature implantation of helium to 7.5 appm He prior to irradiation with 5 MeV iron ions. The results, contained in previous quarterly reports, demonstrated little to no cavity nucleation without helium and significant (> 10^{20} m^{-3}) density of cavities nucleated with pre-implanted helium. This result agreed with available literature stating helium stabilized vacancy clusters and lowered the free energy necessary for stable cavity nuclei. Additional irradiations conducted at 445°C using single ion irradiation (Fe^{2+}) and dual ion irradiation (Fe^{2+}+He^{2+}) with 0.22 appm He/dpa confirmed the necessity of helium to nucleate cavities at 16.6 dpa. While previous studies in literature could nucleate and grow cavities with only iron ion irradiation at higher doses (50 dpa), helium was a necessary component to cavity nucleation at low levels of damage (16.6-20 dpa).

2. **Temperature dependence of microstructural features in dual ion irradiated T91 was determined. The relationship between temperature and cavity evolution in dual ion irradiated T91 exhibited the expected trends of a bell-shaped curve for cavity density and an increasing cavity diameter with temperature.**

The relationship between temperature and dislocation loop evolution in dual ion irradiated T91 followed the expected trends for a ferritic-martensitic alloy. In the temperature regime investigated in this project from 406°C to 570°C in about 15°C-50°C increments, interstitial dislocation loops were expected with a majority of the dislocation loops as part of the a<100> family of dislocation loops. As the temperature increased, interstitial mobility was increased allowing for dislocation loops to grow in diameter but with fewer nucleating dislocation loops. However, at temperatures greater than 510°C, no dislocation loops were observed, consistent with available literature.

The relationship between temperature and cavity evolution in dual ion irradiated T91 exhibited the expected trends of a bell-shaped curve for cavity density and an increasing cavity diameter with temperature. The trend of a bell-shaped curve for cavity density was expected as cavity nucleation is suppressed at low temperatures from the lack of vacancy mobility and suppressed at high temperatures from the thermal emission of vacancies from vacancy clusters. The increase of average cavity diameter with increasing temperature was also expected as the temperature increases the flux of vacancies to cavities through enhanced diffusivity. At these low levels of damage the swelling curve followed the density of cavities and had a total swelling of less than 0.1%, indicating dual ion irradiated T91 is likely still in the nucleation phase of swelling at 35 dpa.

3. **The temperature shift for dual ion irradiation was determined by matching major microstructural features of BOR-60 irradiated T91. A temperature shift of ~60°C for dual ion irradiation was found to result in both a qualitative and quantitative match of cavities in BOR-60 irradiated T91 heat 30176.**

A large achievement of this project was the agreement in irradiated microstructures of the same alloy and heat of alloy between reactor irradiation and ion irradiation. Shifting the temperature of the BOR-60 irradiated T91 heat 30176 about 60°C resulted in both a qualitative and quantitative match of the dislocation loops (Figure 2a.2.2.1) and cavities (Figure 2a.2.2.2) with dual ion irradiated T91 from the same heat of material. Though the agreement extended outside any one particular reactor irradiation condition. The average dislocation loop diameters for the BOR-60 irradiated T91 were found to be within a reasonable error of each other, while the dual ion irradiated T91 exhibited a sharp linear increase with increasing temperature. However, both the dual ion irradiated and reactor irradiated T91 did not form dislocation loops at high temperatures. The dislocation density also extended the same comparison of a sharp change with temperature for ion irradiation and almost negligible change with temperature for neutron irradiation. Similar statements can be made for the average cavity diameter, cavity density, and swelling between reactor and dual ion irradiated T91. The dependence on temperature appeared to be stronger for the high damage rate ion irradiation compared to the low damage rate reactor irradiation.

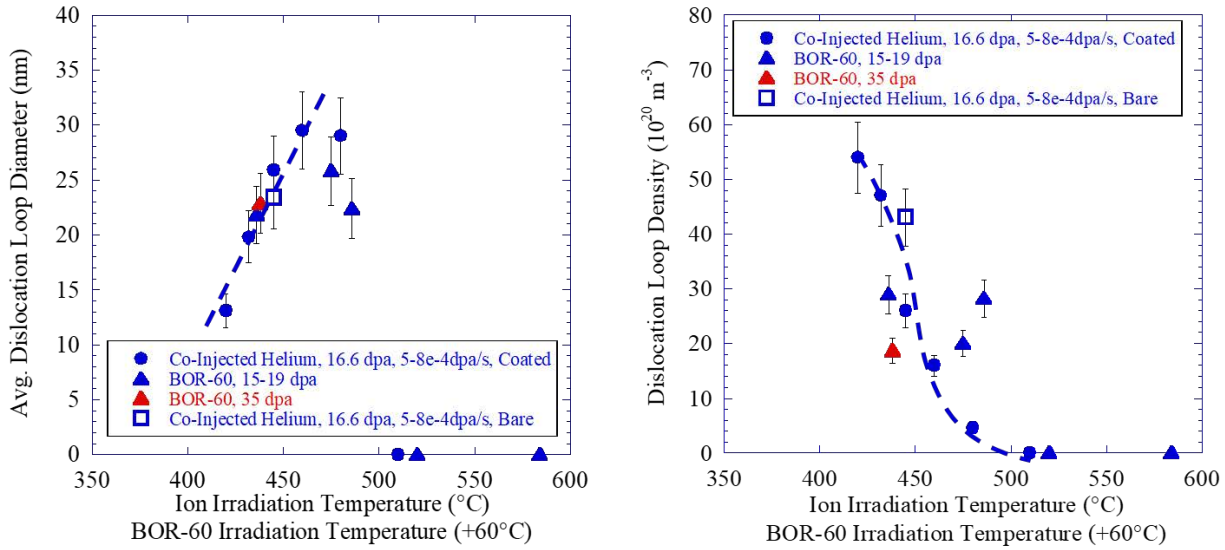

Figure 2a.2.8. A comparison of the average dislocation loop diameter (left) and density (right) as a function of temperature for dual ion irradiated and reactor irradiated (shifted +60°C) T91 heat 30176 with lines drawn to guide the eye.

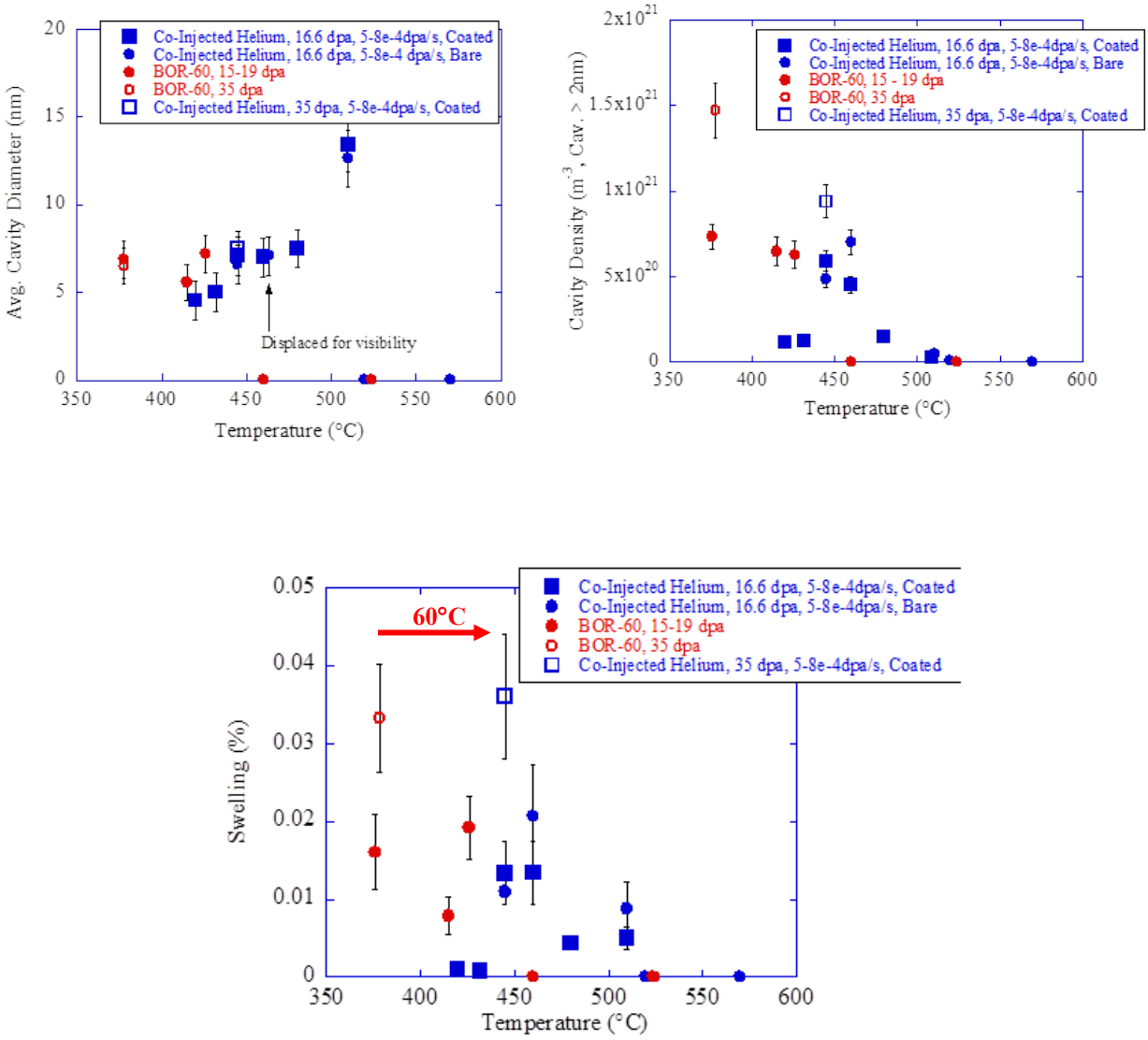

Figure 2a.2.9. A comparison of the average cavity diameter (upper left), density (upper right), and swelling (lower center) as a function of temperature for dual ion irradiated and reactor irradiated T91 heat 30176 with lines drawn to guide the eye.

Alloy HT9

2a.2.3 Ion and BOR60 irradiated HT9 (Ce Zheng, Djamel Kaoumi, North Carolina State University, Elaina Reese, Emmanuelle Marquis, University of Michigan)

1. Irradiation induced dislocation loop population in Ferritic/Martensitic steels T91 and HT9: In-situ ion irradiation vs. Ex-situ (bulk) single ion irradiation vs. neutron irradiation. Observations made on the in-situ irradiations were comparable with the measurements done on the ex-situ irradiation experiments, i.e. a <100> type loops were also found to be the predominant type for both the bulk (ex-situ) ion irradiation and the BOR-60 neutron irradiation F/M steel HT9 at the doses investigated (17-33dpa)

FIB lift-out specimens of Ferritic/Martensitic steels T91 and HT9 were irradiated in-situ up to 20 dpa at 420-470ºC, using 1 MeV Kr^{2+} ions at the IVEM facility, at ANL. The ion flux was set to 6.25×10^{11} ions/cm^2/s corresponding to the dose rate of ~1.07×10^{-3} dpa/s, according to the SRIM-2008 calculation. Sequential TEM images were taken at the same area to quantitatively analyze the evolution of defect size and density vs. irradiation dose. In addition, dynamic observations were performed by video recording during in-situ irradiation. Bulk (ex-situ) ion and neutron irradiations of F/M steels HT9 were also carried out at the MIBL facility, UM and BOR-60 reactor, Russia, respectively. Details of all the irradiations can be found in the quarterly/yearly reports and are summarized in Table 2a.2.3.

Pre-existing microstructures of F/M steels T91 and HT9 include prior austenite grain boundaries (PAGBs) and narrow martensitic lath grains. The initial dislocation density varies from grain to grain. During the in-situ irradiations, the observed trends were similar for both T91 and HT9 at all temperatures [1,2]: (i) black-dot defects started to appear after a small threshold dose, (ii) resolvable loops began to show up at 1 dpa and loop density increased by 2-4 orders of magnitude from 1dpa to 4 dpa, (iii) in the meantime, climb and loss of pre-existing dislocation lines to the free surfaces were observed, resulting in the decrease of dislocation line density in the early stage of irradiation (from 1dpa to 4 dpa), (iv) at higher doses (above 4 dpa), the build-up of new dislocation network was observed along with the loss of dislocation loops to the network formation, resulting in a decrease of dislocation loop density (and an increase of dislocation line density), (v) at the highest doses, the microstructure of the in-situ irradiated samples was dominated by a complex network of dislocation segments created during the irradiation which had no apparent/direct correlation with the initial pre-existing network of dislocation lines which climbed and were lost to the surfaces of the foil in the early stages of the irradiation. The dynamic nature of the formation and evolution of dislocation "segments" / network was evidenced in-situ during the irradiations. Overall, the loop density versus dose showed an inverse trend (increase then decrease) with increasing dose in both in-situ irradiated F/M steels T91 and HT9 at all temperatures.

In order to image dislocation loops and identify their Burgers vector, the on-zone STEM imaging method [3] was performed on both ion and neutron irradiated F/M steels T91 and HT9. The populations of observed **a**/2 <111> and **a** <100> loops are summarized in Table 1. For the in-situ ion irradiations, the proportion of **a** <100> type loops was similar to **a**/2 <111> type loops at 4 dpa, whereas at the higher doses of 10 and 20 dpa (after the decrease of loop number density was

registered) the **a** <100> type loops were found to be the predominant type, which indicated that the decrease of loop density affected more the **a**/2 <111> loop population, with the **a**/2<111> loops possibly being lost (i) to feed the formation of dislocation network or (ii) to interactions resulting in the formation of **a**<100> loops, or (iii) to the free surfaces [1,2].

Moreover, these observations made on the in-situ irradiations were comparable with the measurements done on the ex-situ irradiation experiments, i.e. **a** <100> type loops were also found to be the predominant type for both the bulk (ex-situ) ion irradiation and the BOR-60 neutron irradiation F/M steel HT9 at the doses investigated (17-33dpa) [4]. Details of all the results can be found in the section 2a.2.3 of the IRP Y4Q2 quarterly report.

Table 2a.2.3 Identification of **a** <100> and **a**/2 <111> type dislocation loops in ion irradiated F/M steels T91 and HT9, as well as neutron irradiated F/M steel HT9.

Material	Irradiation type	Dose	Temperature	N° of a <100> loops	N° of a/2 <111> loops	$\frac{\text{a <100>}}{\text{a <100> + a/2 <111>}}$
F/M steel T91	In-situ 1 MeV kr^{2+} ions	4 dpa	470°C	21	25	45.7%
		10 dpa		45	20	69.2%
F/M steel HT9	In-situ 1 MeV kr^{2+} ions	4 dpa	420°C	22	27	44.9%
			470°C	23	24	48.9%
		20 dpa	420°C	35	13	73%
			440°C	33	13	71.7%
			470°C	39	14	74%
	Ex-situ 5 MeV Fe^{2+} ions	20 dpa	420°C	26	11	70.3%
			440°C	13	4	76.5%
			470°C	13	5	72.2%
	BOR-60 neutron	17 dpa	360°C	42	9	82.4%
		33 dpa		80	18	81.6%

1. *C. Zheng and D. Kaoumi, Dose effect on the irradiation induced loop density and Burgers vector in ion-irradiated Ferritic/Martensitic steel HT9, Philosophical Magazine,* ***under review*** *(2018).*
2. *C. Zheng and D. Kaoumi, Mechanisms of dislocation network build-up in Ferritic/Martensitic steels through In-situ irradiation and TEM characterization, Journal of Nuclear Materials,* ***in progress*** *(2018).*
3. *C. M. Parish et al., Journal of Materials Research,* ***30*** *(2015) 1275*
4. *D. Kaoumi and C. Zheng, Neutron irradiation-induced microstructures in Ferritic/Martensitic steel HT9, oral presentation in TMS 2018 conference, Phoenix, AZ, USA*

2. Radiation-induced precipitation and segregation in Ferritic/Martensitic steel HT9: Ex-situ (bulk) ion irradiation vs. neutron irradiation. The observations of the ion irradiations were comparable with those of neutron irradiated HT9, in terms of radiation-induced precipitation of G-phase and radiation-induce segregation in the vicinity of cavities. However, α' (Cr-rich) precipitation were only observed in neutron irradiated HT9, indicating that lower dose rates should be investigated under ion irradiation.

Bulk (ex-situ) single and dual ion beam irradiated and BOR-60 neutron irradiated HT9 samples were characterized by ChemiSTEM and APT techniques (at NCSU and UM respectively). The details of the characterization can be found in the quarterly reports and are summarized in Table 2.

Without irradiation, Thermo-Calc© predicts that Ni/Si/Mn-rich precipitates should not form at temperatures above 400ºC in HT9. This is consistent with the observations done by ChemiSTEM elemental mapping in the non-irradiated areas of the bulk samples irradiated at 420-470ºC (at depths beyond the range of the ions). On the other hand, Ni/Si/Mn-rich precipitates were observed in the irradiated area (depth < 1.5 μm) of all ion irradiated samples at 420-470ºC, except at the low dose of 1 dpa where only elemental segregation at grain boundaries was observed, indicating that the precipitation of Ni/Si/Mn-rich precipitates is dose dependent (i.e. existence of a threshold) [1]. The APT characterization provided an estimate of the stoichiometry of Ni/Si/Mn-rich precipitates, which in addition to the TEM characterization confirmed that G-phase precipitates ($Ni_{16}Si_7Mn_6$) were formed. The TEM characterization coupled with the chemical mapping showed that G-phase precipitates nucleated primarily heterogeneously at defect sinks (i.e. at lath grain boundaries, dislocations and Carbide/Matrix interface) where Ni and Si also segregated, as evidenced by the ChemiSTEM and APT techniques [1]. The defect sinks have a catalytic effect on nucleation due to the possibility of releasing the excess free energy associated with defect sinks. Minor alloy elements such as Ni and Si segregate to the defect sinks under irradiation, leading to the nucleation of the G phase.

In the one dual-beam (Fe +He) irradiated sample examined, the G-phase was also observed to nucleate essentially heterogeneously and spatial correlation of the cavities and the precipitate was found, indicating possible common nucleation sites for the cavities and precipitates.

The observations of the ion irradiations were comparable with those of neutron irradiated HT9, in terms of radiation-induced precipitation of G-phase and radiation-induce segregation in the vicinity of cavities. However, α' (Cr-rich) precipitation were only observed in neutron irradiated HT9, indicating that lower dose rates should be investigated under ion irradiation.

Details of all the results can be found in the section 2a.2.4 of the IRP Y3Q2 and the section 2a.2.3 of the IRP Y3Q3 and Y4Q1 quarterly reports.

Table 2a.2.4. Summary of radiation-induced precipitation (G-phase and α') observed in ion and neutron irradiated F/M steel HT9.

<table>
<tr><th>Material</th><th>Irradiation type</th><th colspan="2">Dose</th><th>Temperature</th><th>G-phase precipitation</th><th>α' precipitation</th></tr>
<tr><td rowspan="6">F/M steel HT9</td><td rowspan="4">Ex-situ 5 MeV Fe^{2+} ions</td><td colspan="2">1 dpa</td><td rowspan="2">470°C</td><td>Not observed</td><td rowspan="4">Not observed</td></tr>
<tr><td colspan="2">10 dpa</td><td rowspan="5">Observed
In addition, heterogeneous precipitation of G-phase also observed at grain boundaries, dislocations and Carbide/Matrix interface</td></tr>
<tr><td colspan="2" rowspan="2">20 dpa</td><td>440°C</td></tr>
<tr><td>420°C</td></tr>
<tr><td>Ex-situ 5 MeV Fe^{2+} ions + He implantation</td><td>17 dpa</td><td rowspan="3">0.22 appm He/dpa</td><td>432°C</td></tr>
<tr><td rowspan="2">BOR-60 neutron</td><td>17 dpa</td><td rowspan="2">360ºC</td><td>Observed</td></tr>
<tr><td>33 dpa</td></tr>
</table>

1. *C. Zheng, D. Kaoumi, et al., Radiation-induced segregation and precipitation behavior in self-ion irradiated Ferritic/Martensitic HT9 steel, Journal of Nuclear Materials,* ***491*** *(2017) 162*
2. *C. Zheng and D. Kaoumi, Radiation-induced swelling and radiation-induced segregation & precipitation in dual beam irradiated Ferritic/Martensitic HT9 steel, Materials Characterization,* ***134*** *(2017) 152*
3. *D. Kaoumi and C. Zheng, Neutron irradiation-induced microstructures in Ferritic/Martensitic steel HT9, oral presentation in TMS 2018 conference, Phoenix, AZ, USA*

3. Guidelines for the selection of irradiation depth for improved cavity swelling analysis in ex-situ dual ion irradiated F/M steel (injected interstitial effect):

Cavity denuded zones near the free surface and at the zone adjacent to the damage peak were found in the (ex-situ) dual ion irradiated HT9 sample (17 dpa and 0.22 appm/He at 432ºC) [1] (Figure 2a.2.10(a)). Interstitials and vacancies near the surface are considered as activated defects which tend to be absorbed by the free surface if not annihilated by recombination with each other. In contrast, a large amount of implanted Fe ions is deposited at the zone adjacent to the damage peak. These injected Fe ions are considered as additional interstitial defects, which reinforces the reduction of vacancies by recombination. As a result, the cavity nucleation is suppressed by the injected interstitials. As shown in Figure 2a.2.10(b), the amount of injected ions deposited in the mid-range area (300-750 nm) is expected to be on much less scale compared to the zones adjacent to the damage peak. For this reason, the cavity swelling analysis must be performed at mid-range (300-750 nm) depth below the irradiated surface to minimize the injected interstitial effect. According to the relationship between dpa and depth, the dpa and swelling percentage can be correlated. The dpa values are estimated by interpolation from SRIM calculations. The swelling rate of dual ion irradiated HT9 is determined by linear fitting of

swelling vs. dpa values (Figure 2a.2.10(c)). Details of all the results can be found in the section 2a.2.3 of the IRP Y3Q3 quarterly report.

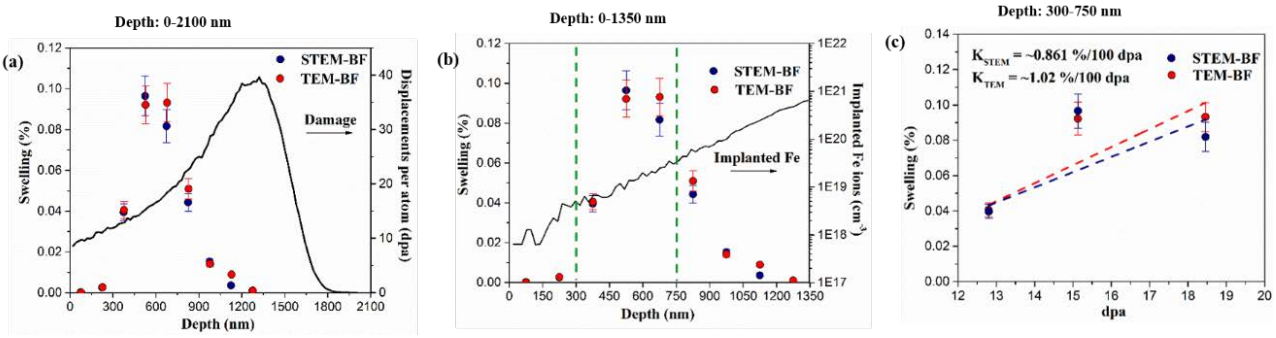

Figure 2a.2.10. Depth-dependent evolution of cavity swelling in dual ion irradiated HT9. The SRIM simulated damage plot is shown as a reference. (b) The implanted Fe ions concentration (ions/cm^{-3}) plot as a function of irradiation depth. (c) Excluding the injected interstitial effect, the mid-range area (300-750 nm) was proposed for cavity swelling analysis.

1. *C. Zheng and D. Kaoumi, Radiation-induced swelling and radiation-induced segregation & precipitation in dual beam irradiated Ferritic/Martensitic HT9 steel, Materials Characterization, **134** (2017) 152*

4. G-phase and α' precipitates were observed BOR60 irradiated HT9 from 376 to 426ºC but they were not observed at 460°C. However, small clusters of Ni, Si, and Mn atoms were observed at 450 ºC in the Dual ion irradiated sample. The number density and radius of G-phase precipitates in BOR60 irradiated HT9 did not show significant variance with increasing temperature or dose. The dual-beam ion irradiated HT9 sample has the highest number density and radius compared to the BOR60 irradiated samples.

The phases observed in the irradiated HT9 alloys include: Ni-Si-Mn-rich G-phase, Cr-rich α' phase, Cu-Fe precipitates, and $M_{23}C_6$-type carbides. Ni and Si enrichment at grain boundaries and the interface of carbides was also observed. G-phase and α' precipitates are inhomogeneously spatially distributed in the 376 to 426ºC BOR60 irradiated samples. Above 426 ºC, the G-phase is observed in the dual beam sample, however very small clusters of Ni, Si, and Mn atoms are observed in the 450 ºC.

The number density and radius of G-phase precipitates in BOR-60 HT9 do not show significant variance with increasing temperature or dose. (~$4x10^{22}$ m^{-3} and ~2 nm). The dual-beam ion irradiated HT9 sample has the highest number density and radius among the samples ($8 \pm 2x10^{22}$ m^{-3} and 3.0 ± 0.9 nm). The compositions of α' precipitates in the HT9 alloys (P027, P028, P035) were calculated using a proxigram method. The α' compositions do not vary significantly with temperature or condition. The α' from P028 (378°C:33 dpa) shows a slight increase in Cr concentration, however more precipitates need to be analyzed to confirm a trend. The number density of α' precipitates increases significantly from samples irradiated at 376 to 426 °C. However, this trend deviates from the expected thermodynamic behavior, where number density

would decrease with increasing temperature as radius increased. In fact, the radius appears consistent in each specimen. This discrepancy could be the result of capturing an APT volume that is close to carbides or grain boundaries which would reduce the number of α' precipitates in the area as Cr segregates to such features rather than form α'.

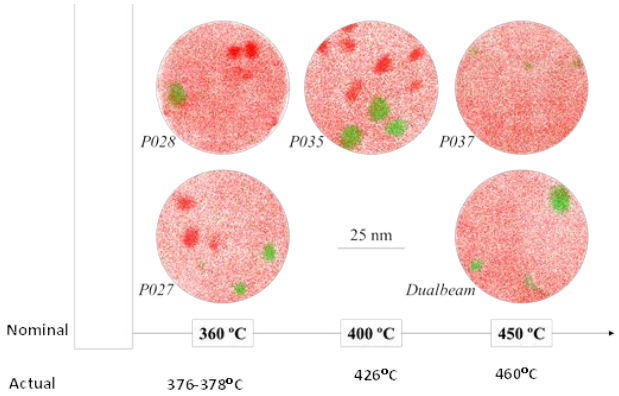

Figure 2a.2.11. Cr (red atoms) , Ni (green atoms), Si, and Mn distributions in HT9 alloys from BOR-60 capsules P027, P028, P035, P037 and a dual beam ion irradiation. From 360 to 426 ºC, Cr atoms form α' precipitates. Ni-Si-Mn precipitates are observed in all alloys except for capsule P037 (16.6 dpa 460 ºC). Atom maps are 10 nm thick.

2b. Thrust 2b: Microstructure Modeling of Irradiated Alloys

2b.1 Modeling of Precipitate Behavior under Ion-irradiations (Morgan Group, University of Wisconsin)

This portion of the work achieved 2 major goals:

1. **Mn-Ni-Si: Developed a detailed cluster dynamics model capable of predicting Mn-Ni-Si precipitate (MSNP) evolution in Fe-based steels under neutron and ion irradiation and used it to understand mechanisms controlling MNSPs in T91. Papers in Ref. [1],[2].**
2. **Fe-Cr: Developed a detailed phase field model capable of predicting α' precipitates in Fe-Cr as a function of flux, composition, and temperature and used it to demonstrate the primary role of ballistic mixing and enhanced recombination in the loss of stable precipitates under high flux ion irradiation. Paper in Ref. [3].**

Mn-Ni-Si: The work used cluster dynamics and integrated data from CALPHAD thermodynamics and measured diffusion kinetics with models for radiation enhanced diffusion and segregation, homogeneous precipitation, and heterogeneous nucleation on cascades and dislocations. Key parameters not available in the literate were fit, e.g., interfacial energies. Precipitate size distributions were predicted for reactor pressure vessel (RPV) steels (primarily funded under a different grant) and validated against atom probe data.[1] The model was then used to predict MNSP evolution under ion irradiation in T91. As shown in Fig. 2b1.1.1, the model demonstrates the essential role of radiation enhanced diffusion (RED) and radiation induced segregation (RIS) in the precipitate number density and size.

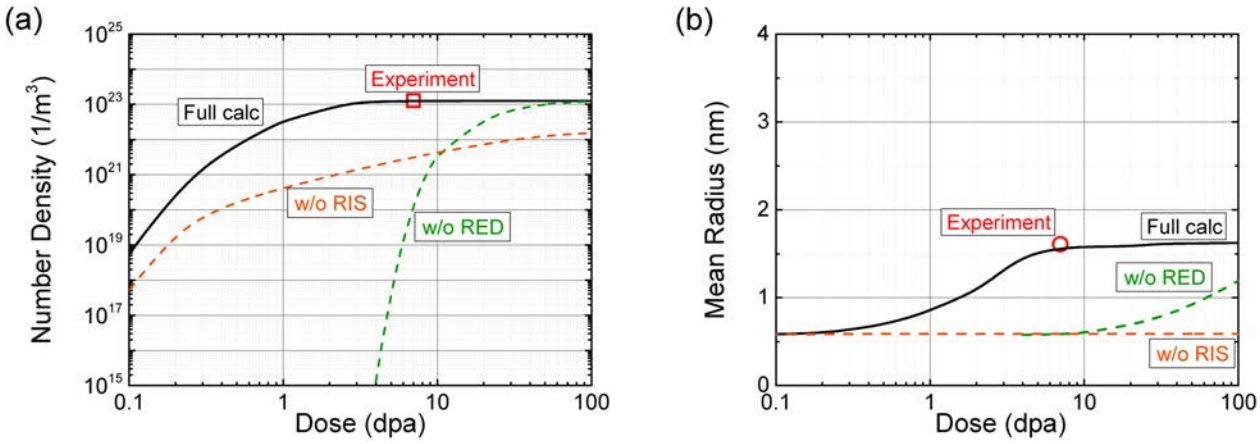

Figure 2b.1.1. Calculation result of the cluster dynamics model showing the (a) number density and (b) mean radius of MNSPs as a function of irradiation dose (dpa) under various conditions, including the full calculations (with dislocations, RIS and RED) and calculations without RIS or RED. The dose rate and temperature are 10^{-5} dpa/s and 400 °C, respectively. The symbols show the values reported by the experiment [4]. This model can be used to predict MNSP evolution in steels under a wide range of irradiation and thermal conditions and support understanding of dominant effects.

Fe-Cr: This work developed the first phase field model that integrated precipitation evolution and ballistic mixing and parameterized it for α' precipitates in Fe-Cr based on CALPHAD, DICTRA, and RED models. The effect of irradiation (with different dose rates) on the phase separation in Fe-15Cr at 290°C is summarized in Figure 2b.1., which shows the histogram plots characterizing the number of computational grids versus composition. The plots for the dose dates of 3.4×10^{-7} and 1×10^{-6} dpa/s exhibit pronounced phase separation with two peaks in each histogram. At a dose rate of 1×10^{-5} dpa/s, no stable α' precipitates form but Cr-rich clusters with a Cr content much lower than that of 3.4×10^{-7} and 1×10^{-6} dpa/s. No Cr-rich clusters form at 1×10^{-4} dpa/s. The result indicates that the critical dose rate causing the α' disappearance is between 10^{-5} and 10^{-4} dpa/s, which corresponds to the general irradiation flux under heavy-ion irradiation with strong cascade generation. This model can be used to investigate flux effects in Fe-Cr and related alloys and demonstrates that changes in ballistic mixing and recombination rates associated with going from neutron to ion irradiation flux can critically affect precipitate evolution.

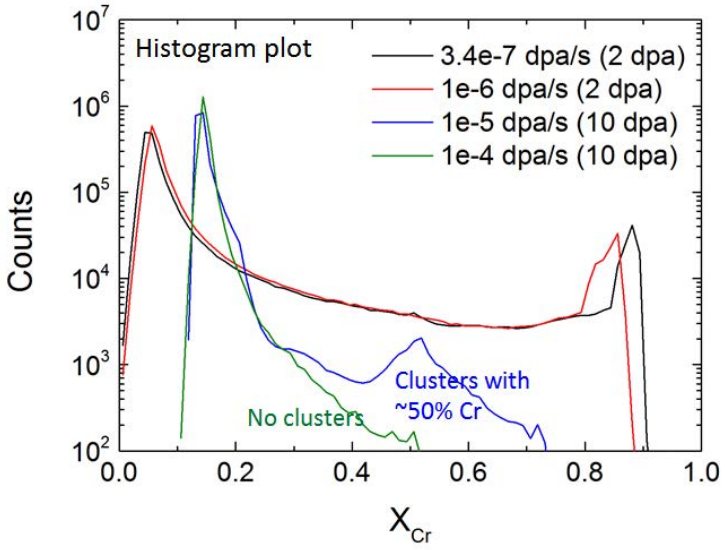

Figure 2b.1.2. Histogram plots showing the number of computational grids versus composition under different levels of irradiation of Fe-15Cr at 290°C.

References

[1] H. Ke, P. Wells, P. D. Edmondson, N. Almirall, L. Barnard, G. R. Odette, and D. Morgan, Acta Materialia **138**, p. 10-26 (2017).

[2] J. H. Ke, H. B. Ke, G. R. Odette, and D. Morgan, Journal of Nuclear Materials **498**, p. 83-88 (2018).

[3] J.-H. Ke, E. R. Anderson, E. A. Marquis, G. R. Odette, and D. Morgan, In preparation (2018).

[4] Z. Jiao, V. Shankar, and G. S. Was, Journal of Nuclear Materials **419**, p. 52-62 (2011).

2b.2 Modeling assessment of tailoring ion irradiation conditions to exactly match neutron irradiation effects (Donghua Xu group, Oregon State/University of Tennessee)

The IRP project is concerned with the feasibility of using ion irradiation to emulate neutron irradiation in terms of producing damage to materials microstructure and mechanical properties. Ion irradiation differs from neutron irradiation in multiple aspects, such as the higher dose rate and the spatial distribution of primary defects. In the case of in-situ ion irradiation in the TEM (Transmission Electron Microscope), the extremely small (tens to a couple hundred nanometer) thickness of a TEM foil and the related surface sink effect on mobile defects constitutes another significant distinction from neutron irradiation and further adds to the complexity of this feasibility problem.

This portion of the work accomplished 2 main results:

1. **BCC Mo: Cluster dynamics modeling of defect cluster evolution in a model, body centered cubic metal demonstrated ability to tailor ion irradiation conditions to exactly match neutron irradiation effects at relatively low temperatures. Paper in Ref. [5].**
2. **BCC Mo: Expanded cluster dynamics modeling to evaluate temperature shift methodology for higher temperatures near 300°C.**

BCC Mo: As reported in our formal journal publication [5], as well as prior IRP Quarterly reports, we have found, through cluster dynamics modeling, that in a low temperature low dose regime, defect evolution across different dose rates in either thin foil ion irradiation or bulk neutron irradiation can be very well matched, by using different irradiation temperatures to counteract the effect of the dose rate variation. Across the thin foil ion irradiation and bulk neutron irradiation, less perfect matching is obtained mainly due to the strong surface sink effect in the thin foil, but the matching can be improved by combining the temperature shift strategy with selection of the central depth in the foil (as opposed to all depths averaged) for matching, or a greater foil thickness (see Fig. 2b.2.1). The better matching to the bulk neutron irradiation with a greater foil thickness in the thin foil irradiation, as well as the the nearly perfect matching across different dose rates within the bulk neutron irradiation scheme alone, indicates that it is quite possible to use bulk ion irradiation to emulate bulk neutron irradiation, within the low temperature and low dose regime.

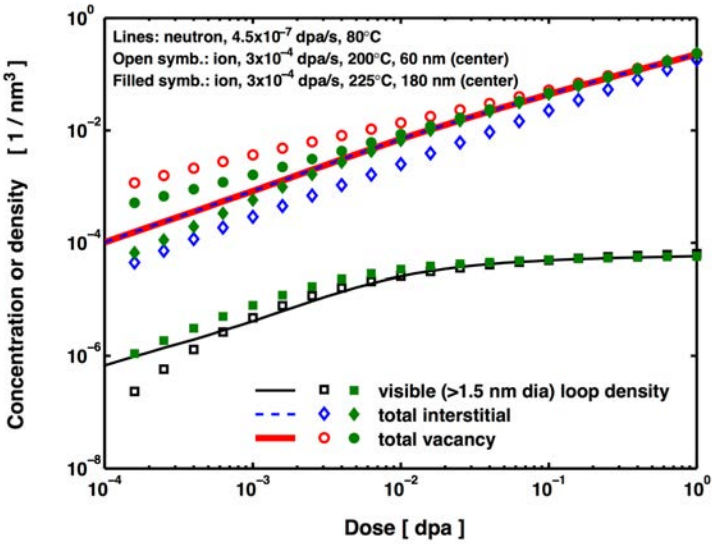

Figure 2b.2.1. Matching defect evolution at the center of 5 MeV Kr ion irradiated 60 nm and 180 nm Mo foils to neutron irradiated bulk Mo.

We subsequently expanded this cluster dynamics modeling to investigate the defect evolution at temperatures around 300°C (near LWR operating temperatures) neutron irradiation, we have found that (see Fig. 2b.2.2) isolated dose rate effect can be reasonably compensated using the temperature shift strategy, if the dose rate varies within one or two orders of magnitude. This suggests that it is still possible to use bulk ion irradiation to match defect evolution under bulk neutron irradiation near LWR operating temperatures, if using a dose rate (on the order of 10^{-6} or 10^{-5} dpa/s) not too far from the neutron irradiation and applying the temperature shift strategy. On the other hand, we have also found that the bulk neutron irradiation at 300 °C is very difficult to be matched with thin foil ion irradiation, due to the magnified surface sink effect on the mobile defects in the high temperature regime.

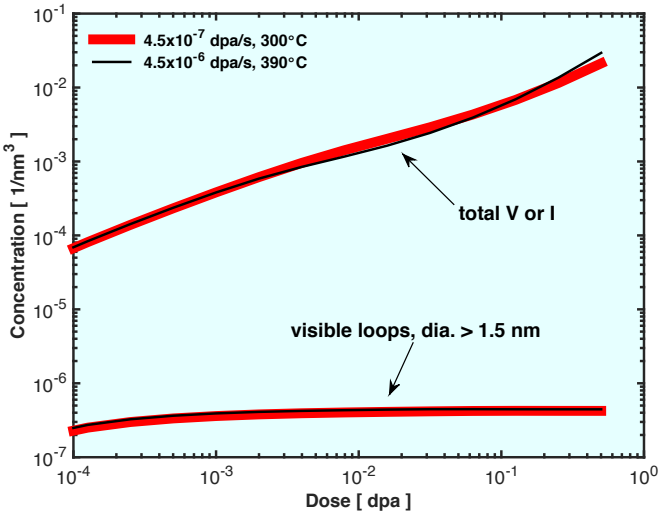

Figure 2b.2.2. Matching defect evolution trajectories of bulk neutron irradiation under different dose rates by using different temperatures.

References

5. D.H. Xu, G. VanCoevering, B.D. Wirth, *Computational Materials Science* **114** (2016) 47-53.

2b.3 Cluster dynamics modeling of void swelling incubation dose (Wirth research group, UTK + VanCoevering and Was, U.Mich)

The IRP project is also concerned with fully understanding the conditions that can lead to void swelling in ferritic-martensitic alloys, as a possible non-saturating radiation effect that could limit the performance of material components in advanced reactors. In the interest of brevity, the spatially-dependent reaction diffusion theory that underpins the cluster dynamics method will not be discussed here, but an extensive description of our approach, computational verification and experimental benchmarking are available in the following reference citations [6-12].

This portion of the modeling accomplished 2 main results:

1. **Cavity bias: Atomistic modeling demonstrate that small vacancy cluster cavities have an intrinsic bias for the preferential absorption of interstitial relative to vacncy defects, particularly at small sizes. This cavity bias can naturally lead to a nucleation barrier against void nucleation. Paper in Ref. [6].**
2. **Fe-Cr alloys under neutron irradiation: Cluster dynamics defect evolution model, incorporating the cavity sink bias quantified in Ref. [6], naturally captures the incubation dose for the onset of void swelling.**

Cavity bias: As reported in our recent journal publication [6], we have performed atomistic molecular statics simulations to investigate the interaction distance leading to spontaneous absorption of self-intersitials, vacancies and helium as a function of void size, where the center of mass of the vacancy cluster is centered on either a lattice site or interstitial position. Figure 2b.3.1 shows the results of such calculations, which clearly show larger interaction distance for interstitials and helium, relative to vacancies. This effect leads to a natural bias in the cavity sink strength for the absorption of self-interstitial atoms relative to vacancies, as shown in Fig. 2b.3.2. Although not presented here, Ref. [6] describes the results of incorporating helium gas pressure within the cavity, for which it was shown that the bias was alleviated in over-pressurized gas bubbles, although the required gas pressure to reach this condition was quite high. As well, our atomistic modeling evaluated several other metals (both BCC and FCC), and concluded that a preference for interstitial capture by relatively small voids was observed for each metal and interatomic potential chosen.

Thus, this work addresses a crucial, but often overlooked aspect of irradiation induced microstructural evolution, namely the interaction of point defects with voids. Our atomistic modeling demonstrated unequivocally that both the spontaneous and effect capture radii between voids and self-interstitial atoms is notably larger than between voids and vacancies. This interaction distance, defined here as the difference between the capture radius and the sum of the radii of the interacting features, does not change as voids become larger. Additionally, the effective capture radius for both vacancy and self-interstitial defects exhibits the expected

temperature dependence. Corresponding, the sink strength scales linearly with this interaction distance for voids, indicating a strong bias for self-interstitial absorption at small void sizes. The implications for cavity nucleation processes are significant.

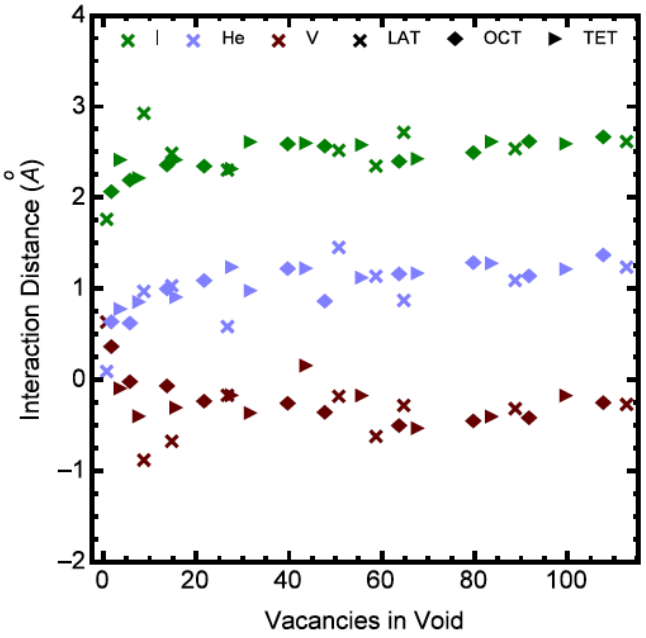

Figure 2b.3.1. Interaction distance for the spontaneous capture of SIAs (I, green), vacancies (V, red cross), or helium (He, light purple) at vacancy clusters of various size with a center of mass on a lattice (lat), versus an octahedral (oct) or tetrahedral (tet) position.

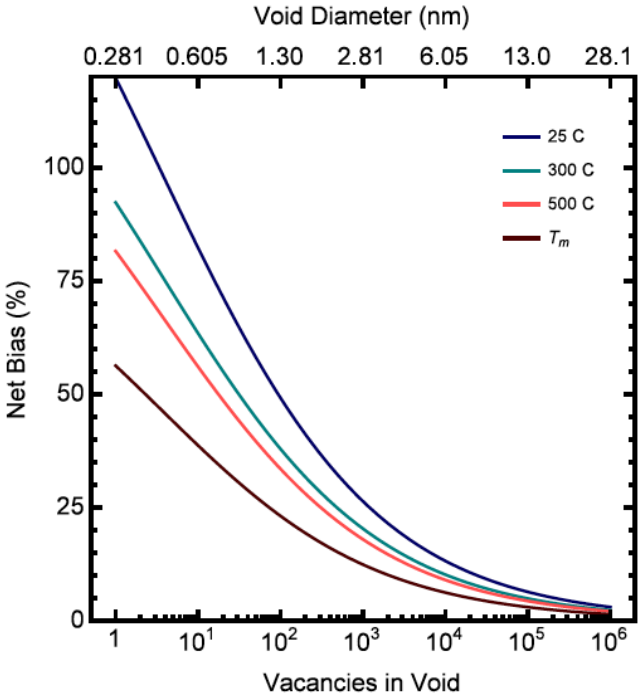

Figure 2b.3.2. Void bias as a function of the number of vacancies in a void, obtained at different temperatures using the results of our atomistic modeling studies presented in Fig. 2b.3.1.

Figure 2b.3.3 shows the impact of incorporating this cluster bias on the resulting void swelling predicted by our cluster dynamics model, as compared to traditional rate theory models, for a range of irradiation temperature and pre-existing heterogeneous cavity nucleation sites. In this work, we have informed our cluster dynamics model with atomistic data on the thermodynamics and kinetics of helium – defect clusters, as well as taken into account the production of defect clusters directly in high-energy displacement cascades, and utilized the aforementioned concept that small vacancy clusters, including those containing an internal gas pressure, are actually biased sinks for absorption of self-interstitial atoms relative to vacancies [6,13]. Our model also incorporates a specified number of heterogeneous nucleation sites for cavities. The family of three curves (up and down triangles, circles, respectively) are predictions of our cluster dynamics model using different densities of heterogeneous nucleation sites, and naturally predict the onset of a critical incubation dose prior to essentially constant swelling rate at an irradiation temperature of 477°C. Our modeling predictions should be compared to the more traditional rate theory solutions (blue and green diamonds) at low versus higher temperature, and with, or without, heterogeneous nucleation sites, respectively. Notably, the traditional rate theory does not predict an incubation dose, nor any dependence of swelling with variation of irradiation temperature from 147 to 427°C, nor a dependence of swelling on homogeneous versus heterogeneous cavity nucleation. However, our results, do naturally predict an incubation dose for swelling, in quite good agreement with experimental observations generated within the IRP project (and literature), although further work is required to make the cluster dynamics model fully predictive.

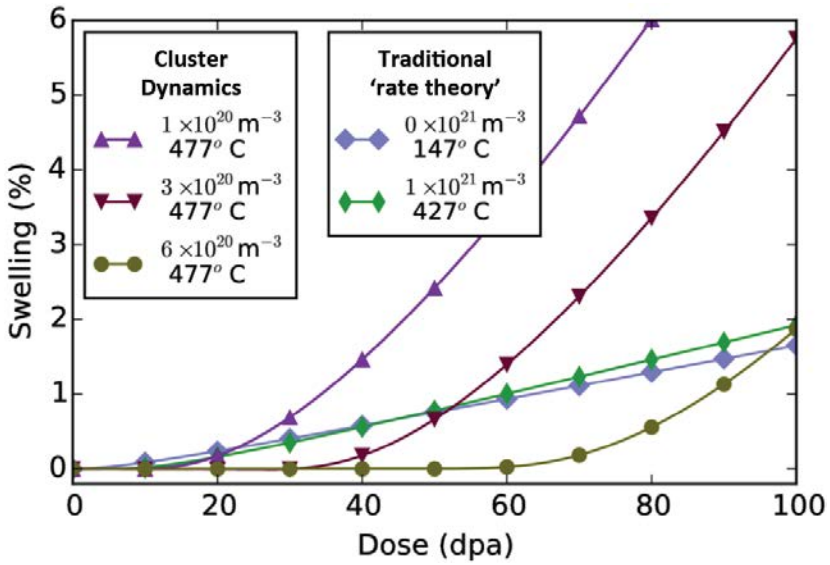

Figure 2b.3.3. Cluster dynamics predictions of swelling (calculated from the predicted cavity size and density) versus radiation dose in an Fe-9%Cr ferritic-martensitic alloy subject to dual (Fe-He) ion irradiation at 477°C (up and down triangles and circles, respectively). Also plotted are the results of a traditional rate theory (blue and green diamonds, respectively) for irradiation temperatures of 147 versus 427°C. The legend also includes the density of heterogeneous cavity nucleation sites that are assumed in each model.

References

[6] A.A. Kohnert, M.A. Cusentino and B.D. Wirth, *Journal of Nuclear Materials* **499** (2018) 480-489.

[7] B.D. Wirth, X. Hu, A. Kohnert, and D. Xu, Journal of Materials Research **30** (2015) 1440-1455.

[8] A.A. Kohnert and B.D. Wirth, Journal of Applied Physics **117** (2015) 154305.

[9] A.A. Kohnert and B.D. Wirth, Journal of Applied Physics **117** (2015) 154306.

[10] X. Hu, D. Xu, T.S. Byun, and B.D. Wirth, Modeling and Simulation in Materials Science & Engineering **22** (2014) 0655002

[11] D. Xu, B.D. Wirth, M. Li, and M. A. Kirk, *Applied Physics Letters* **101** (2012) 101905.

[12] D. Xu, B.D. Wirth, M. Li and M.A. Kirk, *Acta Materialia* **60** (2012) 4286-4302.

[13] M.F. Wehner and W.G. Wolfer, *Phil. Mag A* **52** (1985) 189.

2b.4 Modeling Defect cluster evolution in Alloy 800H (Wirth group, UTK and Motta group, PSU)

The IRP project is also concerned with developing improved understanding and predictive models for defect cluster evolution in advanced austenitic alloys including alloy 800H. During the latter half of the IRP project, we initiated a cluster dynamics modeling activity to predict defect cluster evolution in these alloys, based on the models successfully developed and applied to model bcc metals and ferritic-martensitic alloys. This modeling effort, while not yet fully complete demonstrated the importance of cascade overlap-driven recombination for accurately predicting defect cluster micstructure evolution in irradiated 800H. This effort has begun formulating the initial model for describing the cascade overlap driven recombination rate constants, which will be implemented and tested in follow on research.

This portion of the modeling accomplished one main result:

> **Modeling defect accumulation in irradiated 800H: Cluster dynamics modeling has demonstrated the importance of cascade overlap-induced defect recombination mechanism on the ability to accurately predict defect cluster evolution in irradiated austenitic alloy 800H.**

Using cluster dynamics, we have been simulating radiation damage in 800H from 350^0C to 650^0C up to 100 dpa. We have defined multiple types of defect clusters, including migrating vacancies, migrating interstitials, perfect loops, voids, in addition to faulted dislocation loops of interstitial and vacancy character. For the larger types a grouping scheme is implemented where for groups larger than 50 monomers (single vacancies or interstitial depending on the type), the group widths are set to 0.5nm and follow a 3-order polynomial. The densities and sizes calculated only include observable sizes (about 1 nm in diameter). The binding for each monomer to the type size was calculated using conventional continuum expressions for FCC materials [14]. The distribution of defect sizes produced in sub-cascade damage was produced from matching a continuous distribution to MD simulations in copper [15-17].

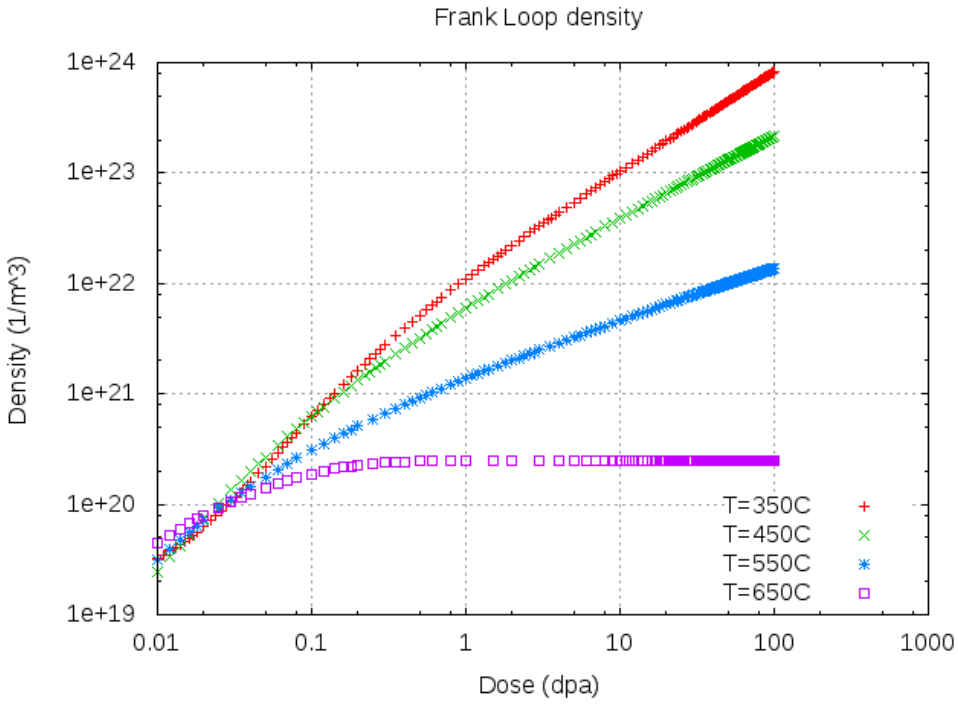

Figure 2b.4.1. Interstitial Frank loop densities as a function of dose for temperatures ranging from 350 to 650°C.

To date, our cluster dynamics models have not included the presence of helium, but the modeling predictions clearly indicate an inability to accurately predict the loop sizes and densities. Figure 2b.4.1 shows representative 800H modeling results of the Frank loop density as a function of irradiation temperature and dose. The lack of density saturation at the lower irradiation temperatures is a concern. One possible cause of these large densities is that current cluster dynamics models lack a way to take into account cascade overlap when the regions that contain damage experiences additional cascade damage. In other words, when damage is generated there should be some way to express in the reaction rate constants the possibility of re-combination, or reactions, that is associated with cascade overlap. Correspondingly, this demonstrates the importance of cascade overlap, and our follow-on research activities will continue to evaluate and experimentally validate the approach we have developed for modeling the reaction rate constant describing recombination

References

[14] Zinkle et.al., Philos. Mag. A, (1987),vol. 55, pg 111
[15] Caturla et. al., J. Nuc. Mater, (2001), 296, pg. 90-100
[16] Bacon et.al., J. Nuc. Mater, (2003), 323, pg. 152-162
[17] T. Diaz de la Rubia and W.J. Phythian, J. Nuc. Mater, (1992), 191-194, pg. 108-115

3. Thrust 3 Accomplishments: Mechanical Properties (Hosemann – UCB, Odette – UCSB, Roberts – Oxford, Preuss – Manchester, Tumey – LLNL, Saleh – LANL)

Major Accomplishments of this Thrust

- **Established correlations between nano- and macro-scale mechanical properties utilizing neutron-irradiated samples from ATR and BOR60. Hardness (*H*) from nanoindentation; tensile yield, flow, and ultimate stresses (σ_y, σ_{flow}, and σ_{uts}) from tensile testing; and shear yield and max (τ_y and τ_{max}) from shear punch testing were all directly measured on the same samples. Methods to extract both tensile and shear macro-scale properties from nanohardness were developed.**
- **Evaluated size effects in both indentation and micro-pillar compression testing utilizing neutron- and ion-irradiated materials over relevant temperature ranges and compared results trends in macro-scale properties.**
- **Developed microstructure-based predictions of hardening on irradiated steels and validated this method utilizing neutron-irradiated sample data.**

3.1 Correlating Nanohardness to Bulk Tensile and Shear Properties Utilizing Neutron-Irradiated Steels – D. Krumwiede, P. Hosemann (UCB), T. Saleh, S. Maloy (LANL), G.R. Odette, and T. Yamamoto (UCSB)

One of the main techniques of emphasis for the mechanical properties team was nanoindentation. This technique is extremely useful for irradiated samples for the following reasons:

- A large number of data points can be generated rapidly from a small volume of simply polished material;
- The length-scale of the test matches well with the scale of ion-irradiation damage layers;
- And there is a large body of historical work focused on micro-indentation and bulk mechanical properties on reactor-irradiated materials.

As such, developing a strong understanding of and confidence in the correlation between nanohardness and both tensile and shear properties became an area of focus. This correlation has been investigated previously using Vickers microhardness. Thus, extending this correlation to the nano length-scale required the direct measure of nanohardness and bulk properties. This was accomplished utilizing two sets of neutron-irradiated steels. LANL performed bulk scale testing on eight samples from ATR for tensile yield, flow, and ultimate stresses (σ_y, σ_{flow}, and σ_{uts}) and thirteen[1] samples from BOR60 for 1% offset and ultimate shear (τ_y and τ_{max}). Afterwards, nanoindentation was performed on all twenty one samples at UCB. All data from these tests can be found in previous quarterly reports.

First, the ATR sample set was used to determine the efficacy of correlating nanohardness to tensile properties. Two empirical correlations – from Milot [1] and Busby [2] – were investigated. After utilizing direct 1000-nm nanohardness (H_{1000}) and characteristic hardness (H_0) from indentation size effect (ISE) analysis [3], it was determined that the calculated tensile property from H_{1000} or H_0 (σ_{ni}) utilizing the Milot correlation best matched σ_{flow}. This result is promising as it indicates the use ISE analysis on ion-irradiated materials (where H_{1000} is not direct measure of irradiated hardness) can still be used to predict tensile properties.

[1] LANL performed shear punch testing on more than thirteen samples, but only thirteen were subsequently shipped to UCB for nanoindentation.

Next, this result was applied to the BOR60 sample set. As there is strong evidence that $\sigma = 1.77\tau$ for irradiated samples [4], the nanohardness data was converted to σ_{ni} using the Milot correlation and then converted again to a calculate shear stress (τ_{ni}) using the 1.77 factor. After correlating τ_{ni} with the measured shear properties, it was determined the only the max shear stress τ_{max} could be reliably predicted with nanohardness. Again, results showed that utilizing H_0 was just as effective as H_{1000}, thus contributing additional confidence that these correlations could be transferred from bulk-type neutron irradiations to shallow ion irradiations.

Going forward, we have shown that nanohardness can accurately predict bulk-scale properties and have a high degree of confidence the same correlations can be applied to ion-irradiated nanohardness data extracted using advanced ISE analysis techniques, such as those presented by IRP contributor Kareer in [5].

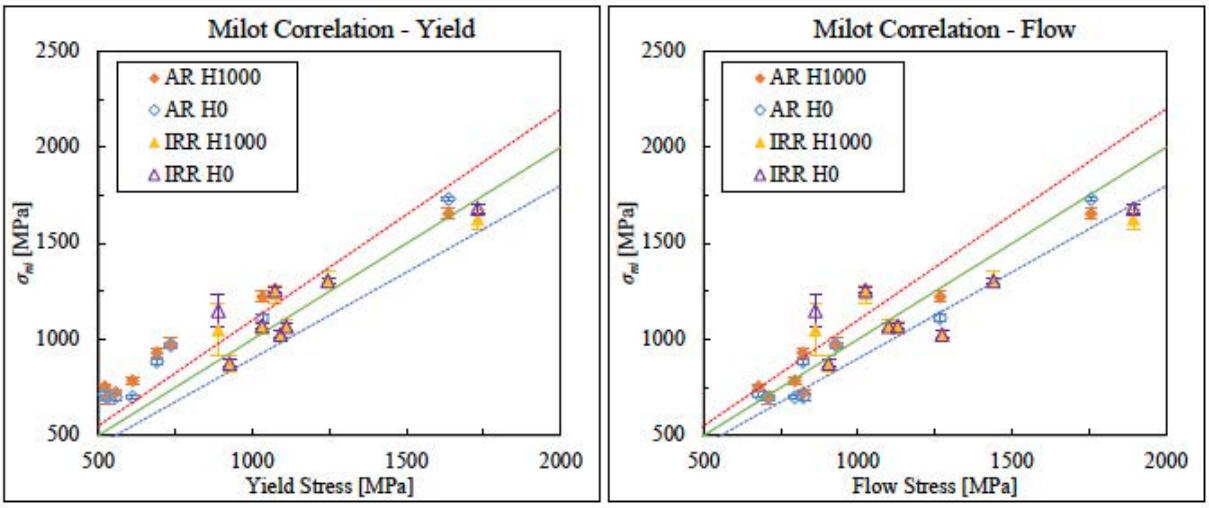

Figure 3.1.1. Comparison of using measured hardness (H_{1000}) versus calculated characteristic hardness (H_0) to predict (left) tensile yield stress ($\sigma_{ni,y}$) and (right) tensile flow stress ($\sigma_{ni,flow}$) using the Milot correlation. Green lines indicates 1:1 agreement, while red/blue lines indicate +/− 10%.

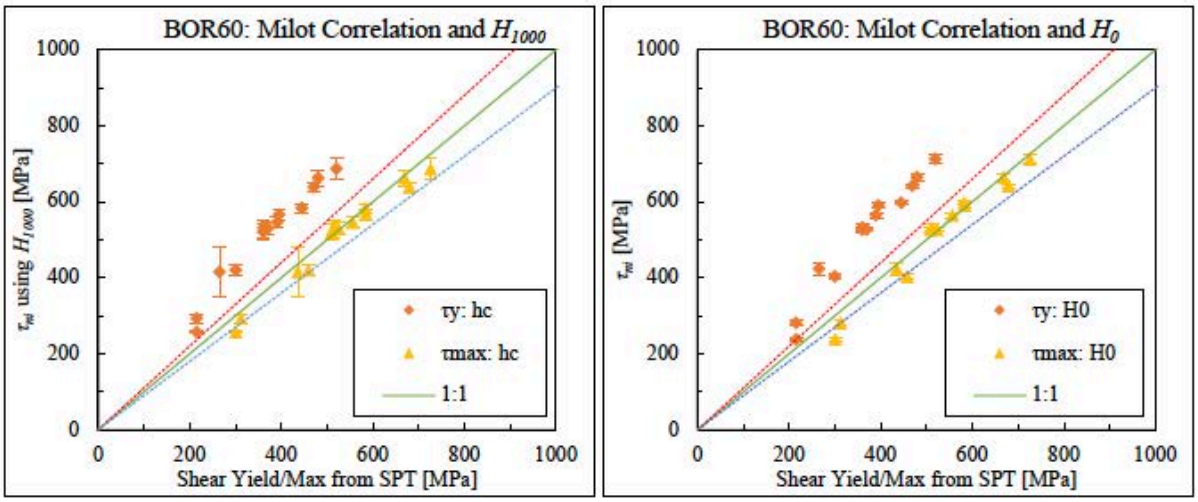

Figure 3.1.2. Plots of comparing shear properties from SPT to those calculated from the Milot correlation and (left) 1000 nm nanohardness H_{1000} or (right) characteristic hardness H_0.

3.1.1 References

[1] T. Milot, MS Thesis, UCSB, 2013.
[2] J.T. Busby, et al., *J. Nucl. Mater.* 336 (2005) 267–278.
[3] W.D. Nix, H. Gao, *J. Mech. Phys. Solids*. 46 (1998) 411–425.
[4] S.A. Maloy, et al., *J. Nucl. Mater.* 417 (2011) 1005–1008.
[5] A. Kareer, et al., *J. Nucl. Mater.* 498 (2018) 274–281.

3.2 Indentation Size Effect (ISE) in Ion-Irradiated Alloys – A. Prasitthipayong and P. Hosemann (UCB)

- Orientation has a strong influence on indentation size effect.
- For the same grain orientation, ISE is less pronounced after irradiation.
- For the same grain orientation and irradiation condition, ISE is less pronounced at high temperatures due to the larger plastic zone size or the storage volume of GNDs.

Figure 3.2.1(a) compares the hardness profiles as a function of indentation depth of the unirradiated and the irradiated 800H. The differences in the hardness drop rates in the two samples suggests different amounts of indentation size effect. Figure 3.2.1(b) shows Nix and Gao plots obtained from the hardness data in Figure 3.2.1(a), illustrating less pronounced size effect after irradiation. The characteristic depth h* reduces from 327 nm to 176 nm after irradiation. h* values are plotted over temperatures in Figure 3.2.1(c). The h* are reduced by 38.8% from 327 nm to 200 nm for the unirradiated 800H and 44.9% from 176 nm to 97 nm for the irradiated 800H in the <111> grain orientation.

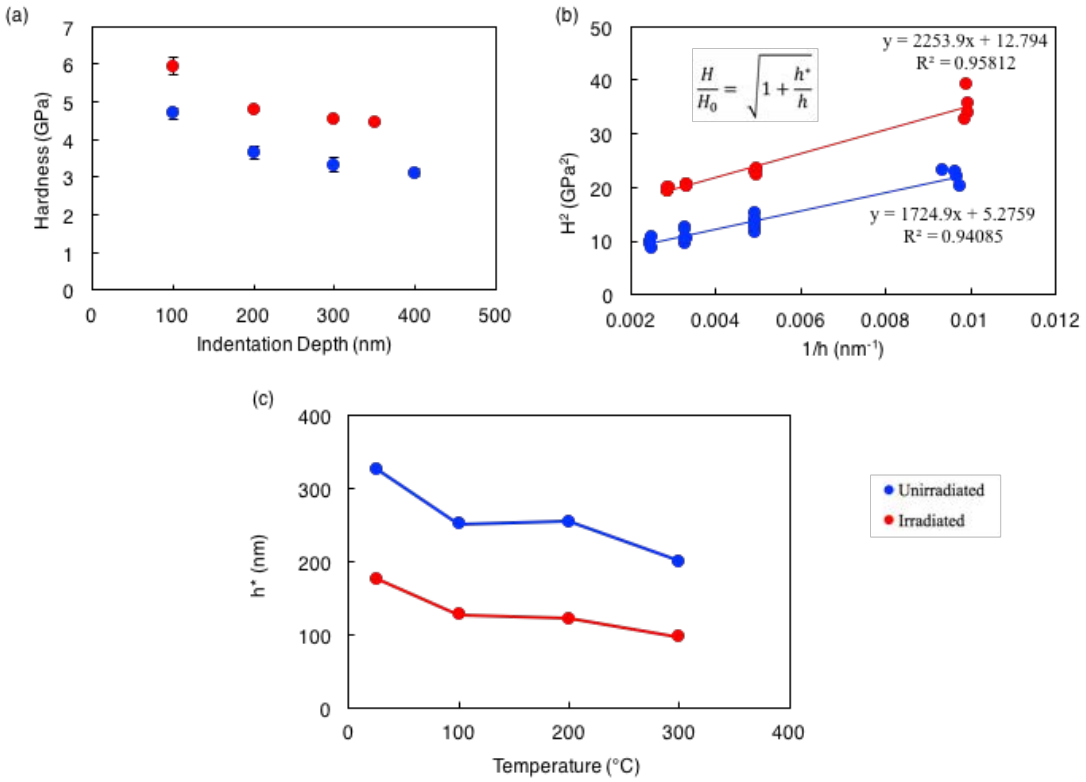

Figure 3.2.1. Comparisons between hardness profiles and indentation size effects in unirradiated and irradiated 800H vs. temperature.

3.3 Sample Size Effect (SSE) in Ion-Irradiated Alloys – A. Prasitthipayong and P. Hosemann (UCB)

- For the same grain orientation, SSE is less pronounced after irradiation.
- For unirradiated 800H, SSE is more significant at high temperatures.
- For irradiated 800H, SSE remains negligible at high temperatures.

A fewer number of load drops were visible in the engineering stress-strain curves of the irradiated micro-pillars than that of the unirradiated micro-pillars. In displacement controlled tests, load drops refer to dislocation activities i.e. slip events [1-2]. This suggests localized, heterogeneous deformation along a few, if not a single, slip planes activated during the compression of the irradiated micro-pillars, implying dislocation channeling which is commonly observed in irradiated alloys [3,4-5]. A power-law dependence of yield stress on micro-pillar diameter (the width of the cross section in this case) is illustrated in Equation 3.3.1 and shown in Figure 3.3.1 [6]. Sample size effect is remarkably less pronounced and become non-existent in the irradiated micro-pillars where $n = 0.09$ versus in the unirradiated counterparts where $n = 0.39$, which agrees well with the previous studies where sample size effect is dependent on initial dislocation density i.e. size effect is less pronounced as initial dislocation density is increased [7].

$$\sigma_y \propto Ad^{-n} \tag{3.3.1}$$

The yield stresses from both unirradiated and irradiated 800H micro-pillars compressed at 300 °C are significantly lower than those obtained at room temperature. This is due to the lower lattice stress and the higher dislocation mobility at elevated temperatures. Nevertheless, the most novel discovery of this work is the influence of temperature on sample size effect in 800H micro-pillars: sample size effect is more pronounced at an elevated temperature. That is, n is 0.21 at room temperature and 0.61 at 300 °C, shown in Figure 3.3.2 (the smallest micro-pillar dimensions are 1x1x2 μm). In the case of the irradiated 800H micro-pillars, sample size effect is nonexistent both at room temperature and at 300 °C, shown in Figure 3.3.3.

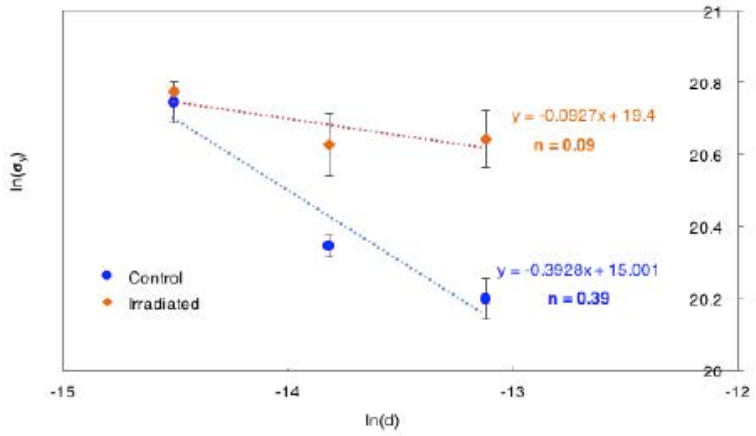

Figure 3.3.1. Sample size effect studies of the unirradiated and irradiated micro-pillars compressed at room temperature (the smallest micro-pillar dimensions are 0.5x0.5x1 μm).

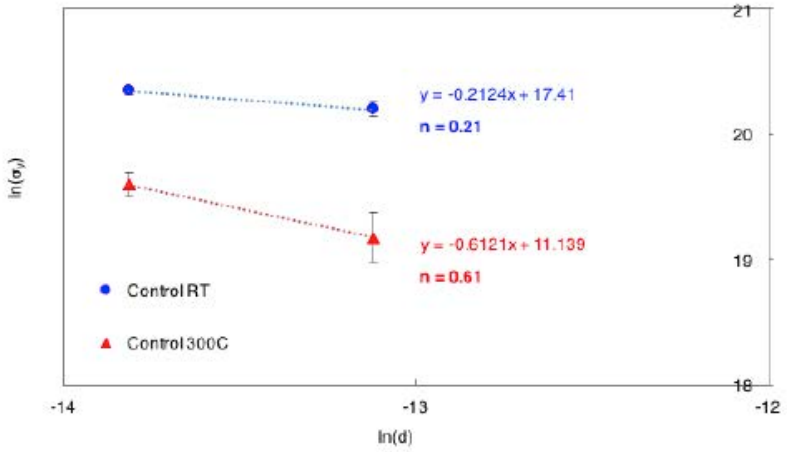

Figure 3.3.2. Influence of temperature on sample size effect in unirradiated 800H micro-pillars (the smallest micro-pillar dimensions are 1x1x2 μm).

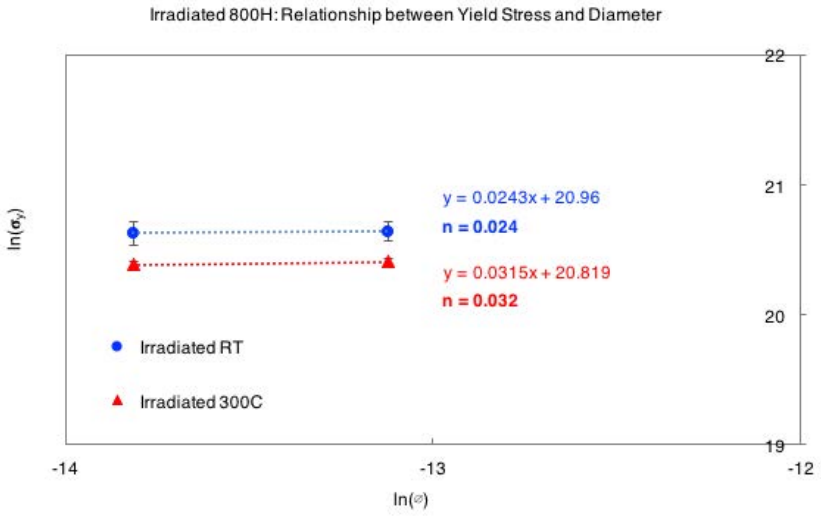

Figure 3.3.3. Influence of temperature on sample size effect in irradiated 800H micro-pillars (the smallest micro-pillar dimensions are 1x1x2 μm).

3.3.1 References

[1] A.M Minor et al., *Nature Materials*. 5 (2006) 697-702.
[2] C. Klingshirn, et al., *Appl. Phys. Lett*. 90 (2007).
[3] Z. Jiao and G.S. Was, *J. Nucl. Mater.* 408 (2011) 246-256.
[4] G.S. Was and P.L. Andresen, *J. Minerals, Metals and Mater Soc*. 44 (1992) 8-13.
[5] T.S. Byun and N. Hashimoto. *J. Nucl. Mater.* 354 (2006) 123-130.
[6] R. Soler, et al., *Acta Materialia.* 81 (2014) 50-57.
[7] S.I. Rao, et al., *Acta Materialia* 56 (2008) 3245-3259.

3.4 Microstructure Based Predictions of Hardening Irradiated Steels – G. R. Odette, T. Yamamoto, P. Wells (UCSB), E. Marquis (UM), D. Bhattacharyya (ANSTO), T. Saleh, and S. Maloy (LANL)

Our objective is to develop well-calibrated, physically based models to predict changes in mechanical properties of irradiated alloys based on microstructural observations. Here we focus on predicting yield stress changes ($\Delta\sigma_y$) that occur under irradiation. The model is based on dispersed barrier (DB) obstacles to dislocation glide. Developing DB hardening models must address two major issues: a) determining the dislocation individual obstacle strength factors (α_i) for all the irradiation modified features (i), including various precipitates (here α' and G-phase), solute-defect cluster complexes (sc), dislocation loops (l), bubbles (b) and voids (v); and, b) parameterizing an appropriate superposition model to determine the net $\Delta\sigma_y$ from the individual hardening contributions of various obstacles (σ_{yi}), including those that are pre-existing in unirradiated steels (σ_{yu}). First, the hardening and observed microstructures for series of Fe-3, 6, 9, 12, 15 and 18Cr model alloys irradiated in UCSB ATR1 experiment were characterized by Vickers microhardness, TEM and APT measurements, and the resulting data was used to least squares fit the α_l, α_{sc} and $\alpha_{\alpha'}$ for dislocation loops, solute clusters and α' precipitates, respectively, in this case without pre-existing obstacles, σ_{yu} = 0 [2]. Figure 1a shows good agreement for the measured versus predicted $\Delta\sigma_y$ (SD = 39) MPa for α_l = 0.2, α_{sc} = 0.17 and $\alpha_{\alpha'}$ = 0.031. In addition to loops, G-phase type Ni-Mn-Si precipitates are observed in steels like T91, along with small bubbles and larger voids. The G-phase precipitate α_p was based on modified Russell-Brown model fit to hardening in irradiated low alloy steels. An extensive microstructural-hardening database and commonly accepted literature values were used to estimate the α_i for voids (α_v = 0.75) and bubbles (α_b = 0.1). BOR60 irradiated T91 hardening and microstructure data were then least square fitted to determine σ_{yu} = 162 MPa. Figure 1.b shows the measured and predicted T91 $\Delta\sigma_y$ which agree each other as well as with saturation hardening trend $\Delta\sigma_y(T)$ in the tempered martensitic steels database assembled by UCSB.

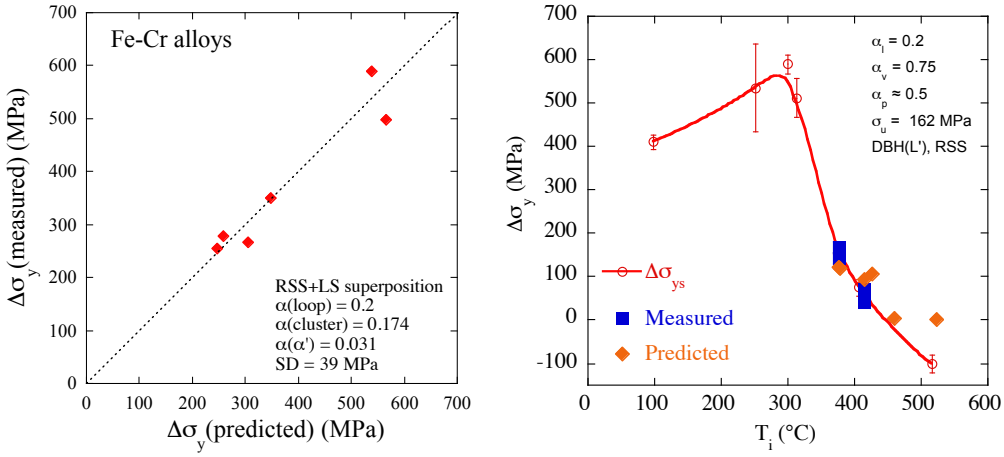

Figure 3.4.1. a) The measured versus predicted $\Delta\sigma_y$ for Fe-3 to 18Cr alloys using best fit obstacle strength factors of α_l = 0.2, α_{sc} = 0.17 and α_α = 0.031; and, b) measured (filled blue squares) and predicted (filled red diamonds) $\Delta\sigma_y$ for T91 irradiated in BOR60, using independently derived a_i values for bubbles (α_b = 0.1), voids (α_v = 0.75 and G-phase precipitates (α_p 0.5) and a best fit σ_{yu} = 162 MPa. The open red circles and solid line show the $\Delta\sigma_y(T)$ trend found in a previous analysis of a large 9Cr steel tempered martensitic database. Predictions agree with the data trend except at the highest *T*.

Thrust 4: Supporting Activities

In addition to technical accomplishments, this IRP also made significant contributions in supporting and furthering the science of ion irradiation and the characterization of ion irradiated Materials. In particular, the following were accomplished:

Ion Irradiation Workshop that established best practices for conducting ion irradiation to study radiation damage in materials, and also to emulate reactor irradiation conditions.

Workshop to establish best practices for transmission electron microscopy characterization of irradiation induced defects.

16 Milestone reports on the following topics:

- **Workshop on Ion Beam Simulation of High Dose Neutron Irradiation**
- **Report on the Best Practices for Transmission Electron Microscopy Characterization of Irradiation Induced Defects**
- **Report on Single Ion Irradiations**
- **Model for Temperature Shift**
- **Characterization of Unirradiated Alloys**
- **Establishment of Multiple Beam Capability at the Michigan Ion Beam Laboratory**
- **Nanoindentation of Ion-Irradiated Samples**
- **Phase Stability in Alloy 800H**
- **Model of Low-dose Precipitation Behavior of Fe-Ni-Mn-Si Model Alloys and Initial Application to High-dose Ni-Mn-Si Precipitation in T91**
- **Void Nucleation**
- **Micro-compression/cantilever test**
- **Comparison of Ion and Neutron Irradiated Microstructures in Alloys T91 and 800H**
- **Micro-compression, Cantilever, and Shear Punch Testing of Irradiated Materials**
- **Microstructure Based Predictions of Hardening in Irradiated T91 Tempered Martensitic Steel**
- **Hardening Model Predictions for IRP BOR60 and Ion Irradiated T91 and Alloy 800H**
- **Model for Microstructure Evolution in Irradiated T91 and 800H**

Engagement of the following collaborators in the conduct of the IRP work scope:

- **TerraPower Inc., U.S.**
- **Electric Power Research Institute, U.S.**
- **Queens University, Canada**
- **University of Manchester, England**
- **University of Oxford, England**
- **CEA, France**
- **Areva, France**

Publications resulted from this project:

[1] P.K. Roy, S. Taller, O. Toader, F. Naab, S. Dwaraknath, G.S. Was, A Multi-Pinhole Faraday Cup Device for Measurement of Discrete Charge Distribution of Heavy and Light Ions, IEEE Trans. Nucl. Sci. (2015) 1–1. doi:10.1109/TNS.2015.2483478.

[2] J.J.H. Lim, M.G. Burke, Heavy Ion Irradiation-induced Microstructural Evolution in the Next Generation Nuclear Material – Alloy 800H, Microsc. Microanal. 22 (2016) 1482–1483. doi:10.1017/S1431927616008254.

[3] D. Xu, G. VanCoevering, B.D. Wirth, Defect microstructural equivalence in molybdenum under different irradiation conditions at low temperatures and low doses, Comput. Mater. Sci. 114 (2016) 47–53. doi:10.1016/j.commatsci.2015.11.045.

[4] K.G. Field, S. Taller, C.J. Ulmer, Z. Jiao, T.A. Saleh, A.T. Motta, G.S. Was, Application of NSUF Capabilities Towards Understanding the Emulation of High Dose Neutron Irradiations with Ion Beams, in: Trans. Am. Nucl. Soc., San Francisco, CA, 2017: pp. 1–2.

[5] E.R. Anderson, E.A. Marquis, A Snapshot of the Microstructural Evolution of Alloy 800H Under Heavy Ion Irradiation, Microsc. Microanal. 23 (2017) 2254–2255. doi:10.1017/S143192761701193X.

[6] A.A. Kohnert, B.D. Wirth, Grouping techniques for large-scale cluster dynamics simulations of reaction diffusion processes, Model. Simul. Mater. Sci. Eng. 25 (2017) 15008. doi:10.1088/1361-651X/25/1/015008.

[7] E.R. Reese, M. Bachhav, P. Wells, T. Yamamoto, G. Robert Odette, E.A. Marquis, On α′ precipitate composition in thermally annealed and neutron-irradiated Fe- 9-18Cr alloys, J. Nucl. Mater. (2017). doi:10.1016/j.jnucmat.2017.12.036.

[8] A. Prasitthipayong, S.J. Vachhani, S.J. Tumey, A.M. Minor, P. Hosemann, Indentation size effect in unirradiated and ion-irradiated 800H steel at high temperatures, Acta Mater. (2017). doi:10.1016/j.actamat.2017.11.001.

[9] C. Zheng, D. Kaoumi, Radiation-induced swelling and radiation-induced segregation & precipitation in dual beam irradiated Ferritic/Martensitic HT9 steel, Mater. Charact. 134 (2017) 152–162. doi:10.1016/j.matchar.2017.10.019.

[10] O. Toader, F. Naab, E. Uberseder, T. Kubley, S. Taller, G. Was, Technical Aspects of Delivering Simultaneous Dual and Triple Ion Beams to a Target at the Michigan Ion Beam Laboratory, Phys. Procedia. 90 (2017) 385–390. doi:10.1016/j.phpro.2017.09.039.

[11] D. Kaoumi, C. Zheng, Microstructure Characterization of Ion-irradiated Ferritic/Martensitic HT9 Steel, Microsc. Microanal. 23 (2017) 2214–2215. doi:10.1017/S1431927617011734.

[12] S. Taller, D. Woodley, E. Getto, A.M. Monterrosa, Z. Jiao, O. Toader, F. Naab, T. Kubley, S. Dwaraknath, G.S. Was, Multiple ion beam irradiation for the study of radiation damage in materials, Nucl. Instruments Methods Phys. Res. Sect. B Beam Interact. with Mater. Atoms. 412 (2017) 1–10. doi:10.1016/j.nimb.2017.08.035.

[13] G.S. Was, S. Taller, Z. Jiao, A.M. Monterrosa, D. Jennings, T. Kubley, F. Naab, O. Toader, E. Uberseder, Resolution of the Carbon Contamination Problem in Ion Irradiation Experiments, Nucl. Instruments Methods Phys. Res. Sect. B-Beam Interact. with Mater. Atoms. 412 (2017) 58–65.

[14] C. Zheng, M.A. Auger, M.P. Moody, D. Kaoumi, Radiation induced segregation and precipitation behavior in self-ion irradiated Ferritic/Martensitic HT9 steel, J. Nucl. Mater. 491 (2017) 162–176. doi:10.1016/j.jnucmat.2017.04.040.

[15] X. Hu, K.G. Field, S. Taller, Y. Katoh, B.D. Wirth, Impact of neutron irradiation on thermal helium desorption from iron, J. Nucl. Mater. 489 (2017) 109–117. doi:10.1016/j.jnucmat.2017.03.034.
[16] E.R. Reese, N. Almirall, T. Yamamoto, S. Tumey, G. Robert Odette, E.A. Marquis, Dose rate dependence of Cr precipitation in an ion-irradiated Fe18Cr alloy, Scr. Mater. 146 (2018) 213–217. doi:https://doi.org/10.1016/j.scriptamat.2017.11.040.
[17] A.A. Kohnert, M.A. Cusentino, B.D. Wirth, Molecular statics calculations of the biases and point defect capture volumes of small cavities, J. Nucl. Mater. 499 (2018) 480–489. doi:10.1016/j.jnucmat.2017.12.005.
[18] C.J. Ulmer, A.T. Motta, Characterization of faulted dislocation loops and cavities in ion irradiated alloy 800H, J. Nucl. Mater. 498 (2018) 458–467. doi:10.1016/j.jnucmat.2017.11.012.
[19] A. Kareer, A. Prasitthipayong, D. Krumwiede, D.M. Collins, P. Hosemann, S.G. Roberts, An analytical method to extract irradiation hardening from nanoindentation hardness-depth curves, J. Nucl. Mater. (2018). doi:10.1016/j.jnucmat.2017.10.049.
[20] Z. Jiao, S. Taller, K.G. Field, G. Yeli, M.P. Moody, G.S. Was, Microstructure Evolution of T91 Irradiated in the BOR60 Fast Reactor, J. Nucl. Mater. Submitted (2018).
[21] Microstructures of Alloy 800H after heavy ion and neutron irradiations, Elaina Reese, Joven H Lim, Christopher Ulmer, Arthur Motta, M Grace Burke, Emmanuelle A Marquis, in preparation.
[22] A.A. Kohnert and B.D. Wirth, "Cluster dynamics models of irradiation damage accumulation in ferritic iron. II. Effects of reaction dimensionality", *Journal of Applied Physics* **117** (2015) 154306
[23] A.A. Kohnert and B.D. Wirth, "Cluster dynamics models of irradiation damage accumulation in ferritic iron. I. Trap mediated cluster diffusion", *Journal of Applied Physics* **117** (2015) 154305
[24] D. Bhattacharyya, T. Yamamoto, P. Wells, E. Marquis, M. Bachhav, Y. Wu, J.Davis, N. Cunningham, A. Xu and G. R. Odette, Microstructural changes and their effect on hardening in neutron irradiated Fe-Cr alloys, in preparation
[25] T. Yamamoto and G. R. Odette, Development of a Multi-feature Microstructure-Irradiation Hardening Model for Tempered Martensitic Steels: Application to T91 and HT9, in preparation
[26] D.L. Krumwiede, M.D. Abad, T.A. Saleh, S.A. Maloy, G.R. Odette, T. Yamamoto, et al., Initial studies on the correlation of nanohardness to engineering-scale properties of neutron-irradiated steels, in: Int. Congr. Adv. Nucl. Power Plants, ICAPP 2016, San Francisco, 2016: pp. 224–229.
[27] M. Ayanoglu, A. T. Motta, In-situ study: Faulted Loop and Void Behavior in Single Beam Bulk Irradiated Fe-21Cr-32Ni Model Alloy, Transactions of the ANS Winter Meeting 2017.
[28] M. Ayanoglu, A. T. Motta, Microstructural evolution of the 21Cr32Ni model alloy under irradiation, submitted to J. Nucl. Mat. (2018).
[29] M. Ayanoglu, A.T. Motta, Evolution of radiation damage during in-situ irradiation of 21Cr32Ni model alloy- in preparation for submission to J. of Nucl. Mater.
[30] M. Ayanoglu, C. J. Ulmer, A. T. Motta, Comparison of radiation damage behavior of 21Cr32Ni model alloy and 800H, In preparation for submission to J. of Nucl. Mater.

[31] D.L. Krumwiede, T. Yamamoto, T.A. Saleh, S.A. Maloy, G.R. Odette, P. Hosemann, Direct comparison of nanoindentation and tensile test results on reactor-irradiated materials, J. Nucl. Mater. (2018), doi: 10.1016/j.jnucmat.2018.03.021.
[32] J. H. Ke, P. Wells, P. D. Edmondson, N. Almirall, L. Barnard, G. R. Odette, and D. Morgan, Thermodynamic and kinetic modeling of Mn-Ni-Si precipitates in low-Cu reactor pressure vessel steels, Acta Materialia **138**, p. 10-26 (2017).
[33] J. H. Ke, H. B. Ke, G. R. Odette, and D. Morgan, Cluster dynamics modeling of Mn-Ni-Si precipitates in ferritic-martensitic steel under irradiation, Journal of Nuclear Materials **498**, p. 83-88 (2018).
[34] Z. Jiao, S. Taller, K. Field, G. Yeli,, M. P. Moody, G. S. Was, "Microstructure Evolution of T91 irradiated in the BOR60 Fast Reactor," J. Nucl. Mater. 504 (2018) 122-134.
[35] J.-H. Ke, E. R. Anderson, E. A. Marquis, G. R. Odette, and D. Morgan, Flux effects in precipitation under irradiation – simulation of Fe-Cr alloys, In preparation (2018).